JOURNAL OF GEOPHYSICAL RESEARCH, VOL. 101, NO. B5, PAGES 11,401–11,425, MAY 10, 1996

Magnetic potential and magnetization contrasts of Earth's lithosphere

J. Arkani-Hamed

Earth and Planetary Sciences, McGill University, Montréal, Québec, Canada

J. Dyment[1]

Centre National de la Recherche Scientifique URA 1278, Université de Bretagne Occidentale Brest, France

Abstract. An inversion technique is developed in order to transform a global scalar magnetic anomaly map into a global magnetic susceptibility contrast map which delineates the magnetic characteristics of the lithosphere. The inversion involves two stages. In the first stage, a scalar magnetic anomaly map is transformed into a magnetic potential map. This stage requires no simplifying assumption, and it provides a means to upward/downward continue global scalar magnetic anomaly maps. In the second stage, the potential map is inverted into a magnetic susceptibility contrast map of the lithosphere based on the assumption that the magnetization is of induced origin. The magnetization of the continental crust that gives rise to satellite magnetic anomalies is largely of induced origin. It is also shown that the magnetization direction of the oceanic lithosphere does not differ significantly from the direction of the present core field, except in a few limited areas, supporting the assumption made about the induced magnetization of the lithosphere. The technique is applied to the scalar magnetic anomaly map of Earth derived using POGO and Magsat data. The resulting susceptibility contrasts directly correlate with geological features and better delineate small-scale features due to the enhancement of the higher-degree harmonics compared to the lower-degree ones.

Introduction

The global magnetic anomaly maps of the Earth derived from POGO data [*Regan et al.*, 1975; *Langel*, 1990] and Magsat data [e.g., *Langel et al.*, 1982a; *Yanagisawa and Kono*, 1985; *Arkani-Hamed and Strangway*, 1986; *Cain et al.*, 1989; *Cohen and Achache*, 1990; *Ravat et al.*, 1995] by different authors using different techniques show good correlation over well-defined anomalies with amplitudes greater than 4 nT. Most recently, *Arkani-Hamed et al.* [1994] have derived two global scalar magnetic anomaly maps of Earth at the satellite altitude of 400 km on the basis of POGO and Magsat data using two different selection criteria, which involve a trade-off of signal to noise ratio and signal power retained. Figure 1 shows the map derived using the stringent selection criteria and consists of spherical harmonics of degree 15-60. There are strong magnetic anomalies, both positive and negative, over the continents and some well-defined anomalies over the oceanic areas. The map reveals the magnetic anomalies with greater accuracy as estimated from their standard deviations [see *Arkani-Hamed et al.*, 1994, Figure 6b], suggesting that the anomalies with amplitudes greater than 2 nT certainly originate due to lateral variations in the magnetization of the lithosphere.

The next step is to identify geological features associated with these anomalies. However, there is no direct correlation between magnetic anomalies and the magnetic source bodies on a global scale. This is largely due to the fact that the direction and intensity of the core field drastically change over the globe. A body with an induced magnetization produces a strong and positive magnetic anomaly directly above itself when it is located near a geomagnetic pole but a relatively weak and negative anomaly when it is placed near the geomagnetic equator. The magnetic anomaly is shifted toward the geomagnetic equator relative to the source body when the body is located at midlatitudes.

To overcome these difficulties, it is necessary to convert the magnetic anomalies into magnetization contrasts which correlate directly with the magnetic source bodies. This is usually achieved either by forward mod-

[1] Formerly at Earth and Planetary Sciences, McGill University, Montréal, Québec, Canada.

Paper number 95JB03537.
0148-0227/96/95JB-03537$09.00

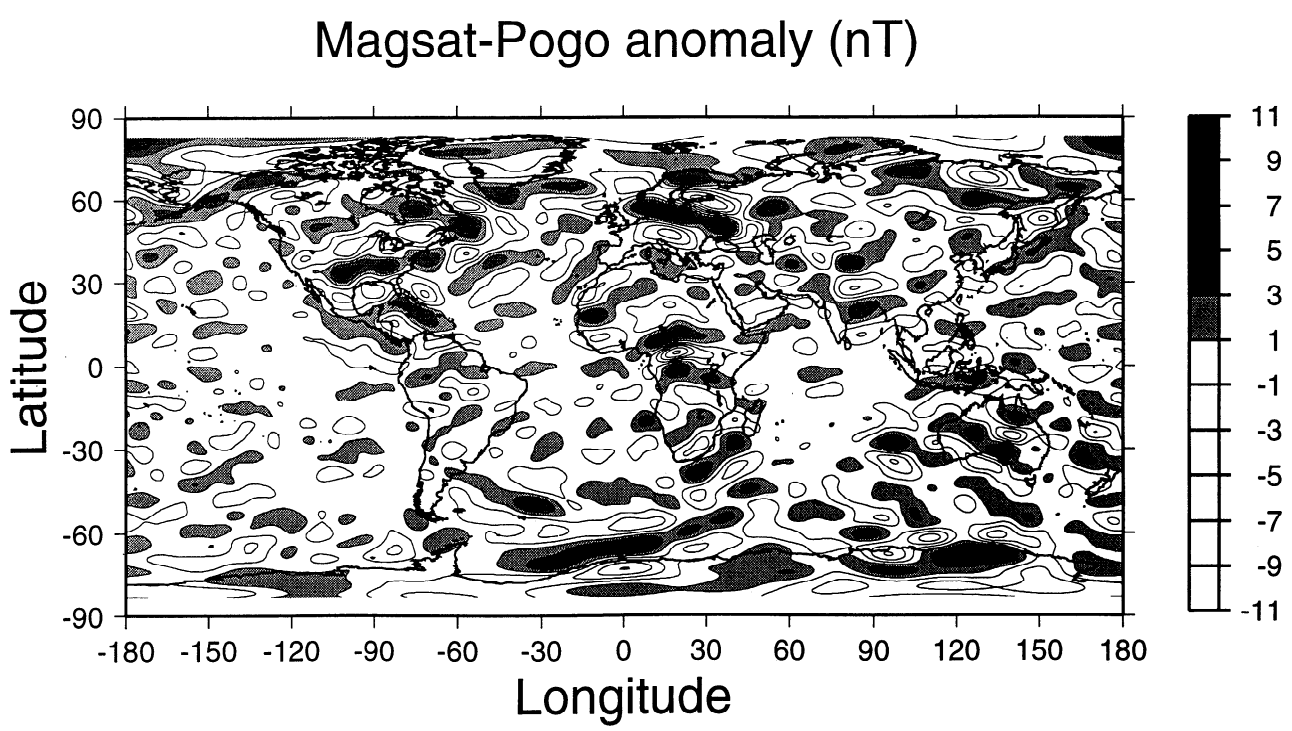

Figure 1. Scalar magnetic anomaly of Earth at 400 km altitude derived by using the stringent criteria [after *Arkani-Hamed et al.*, 1994]. Positive anomalies are shaded in all magnetic maps.

eling or inversion techniques. The forward modeling technique is more suitable for regional anomaly maps with limited number of relatively simple source bodies. It has the advantage that the dimensions of the bodies are usually estimated from other geological and geophysical observations. The inversion technique, especially that applied on a global scale, usually relies on the characteristics of the magnetic anomalies. *Mayhew* [1979] applied the equivalent source technique to invert satellite magnetic anomalies into crustal magnetization by determining an array of magnetic dipoles put on Earth's surface which give rise to the observed magnetic anomalies. The inversion became unstable when dipole spacing was reduced below about 300 km [*Mayhew et al.*, 1980]. *Langel* [1990] adapted the equivalent source technique to POGO data on a global scale by dividing Earth's surface into overlapping segments. He used the principle component analysis in order to suppress instability at and near the geomagnetic equator. *Arkani-Hamed and Strangway* [1985b] developed a technique to invert a global scalar magnetic anomaly map into a global magnetic susceptibility contrast map using the spherical harmonic domain analysis. The technique was based on two simplifying assumptions: 1) the core field was replaced by its dipole component, and 2) the lithospheric magnetization was assumed to be in the direction of the dipole component. In the continental areas an intrusive body large enough to produce a magnetic anomaly at satellite altitudes, with an amplitude above the noise level of 2 nT, cools very slowly through the range of the magnetic blocking temperatures of the consisting minerals. During this long period the core field may change its polarity several times, and different parts of the intrusive may acquire natural remanent magnetization (NRM) in opposite directions and thus cancel the magnetic field of each other as observed at satellite altitudes [*Arkani-Hamed and Celetti*, 1989]. The volcanic extrusives formed in a short time span may acquire strong NRM and produce pronounced aeromagnetic anomalies at low altitudes. However, generally, they are very thin compared to satellite altitudes, and their magnetic anomalies at those altitudes are usually smaller than the error limit of satellite magnetic anomalies. It is therefore plausible to assume that the NRM has little contribution to the satellite magnetic anomalies of the continents and that the anomalies mainly arise from the lateral variations in the induced magnetization of the lithosphere, and perhaps only the crust. The viscous magnetization acquired since the last core field polarity reversal is essentially in the direction of the present core field and cannot be distinguished from induced magnetization on the basis of magnetic anomaly analysis alone. Therefore the induced magnetization referred to in this paper includes this viscous magnetization, and thus it is essentially an effective induced magnetization.

The oceanic lithosphere carries both NRM and induced magnetization. Due to strong attenuation with altitude, the seafloor spreading magnetic anomalies do not significantly contribute to satellite anomalies except when a given polarity dominates, such as the Cretaceous quiet zones (KQZ) which were formed during a long (about 35 m.y.) normal polarity period of the core field and create well-defined positive magnetic anoma-

lies at satellite altitudes [e.g., *LaBrecque and Raymond,* 1985; *Fullerton et al.,* 1989, 1994; *Pal,* 1990]. Being almost uniform laterally, the induced magnetization of normal oceanic lithosphere does not create appreciable magnetic anomalies. The prominent magnetic anomalies associated with oceanic plateaus mainly arise from the induced magnetization of their thickened crust [e.g., *LaBrecque and Cande,* 1984; *Johnson,* 1985; *Frey,* 1985; *Bradley and Frey,* 1988; *Toft and Arkani-Hamed,* 1992]. It is desirable to take into account both remanent and induced magnetization of the oceanic lithosphere when inverting a global magnetic anomaly map into a magnetization contrast map. One possible procedure is to subtract the magnetic anomalies due to the NRM from the observed anomalies and regard the residual as being of induced origin. *Dyment and Arkani-Hamed* [1994] made an attempt in this direction. However, the lack of adequate paleopole position for large oceanic areas, such as the western Pacific, made it difficult to determine the NRM direction and incorporate it into the inversion process. Moreover, the satellite magnetic anomalies of the Atlantic KQZ show appreciable anomalous skewnesses of about 35°-45° [*LaBrecque and Raymond,* 1985]. Whether such a skewness is a characteristic of the KQZs elsewhere is not clear. The KQZs in the South Atlantic are adjacent to continental areas, and it is difficult to determine their skewnesses accurately. The KQZ of the Pacific has a large horizontal extension and does not produce an anomaly at satellite altitude except near its edges [*Toft and Arkani-Hamed,* 1992]. As will be shown in the present paper the NRM direction of the oceanic lithosphere does not significantly differ from that of the present core field, except in a few limited areas. Therefore we assume the magnetization in the oceanic lithosphere to be in the core field direction, recognizing that the assumption must be relaxed once paleopole positions of those areas are better specified and the source of the anomalous skewness of the KQZ is identified.

One of the goals of this paper is to develop an inversion technique in order to determine the magnetic potential directly from the scalar magnetic anomalies using the entire core field model rather than its dipole component as adopted by *Arkani-Hamed and Strangway* [1985b]. The advantage of this approach is that the scalar magnetic anomalies derived from satellite data have much lower error limits than the vector field anomalies, largely due to the attitude uncertainties. For Magsat, the scalar anomalies have errors less than 2 nT, well below the amplitude of the anomalies, whereas the attitude uncertainty alone introduced about 5 nT error into the vector data and increased their error limit to over 6 nT [*Langel et al.,* 1982b]. Although subsequent data processing reduces the error limit [see, e.g., *Ravat et al.,* 1995], the error of the processed vector data is still comparable to the amplitudes of the vector anomalies. Vector data from the Oersted mission (to be launched in early 1997) are expected to have 3-5 nT error limit, whereas its scalar data will have an error less than 1.3 nT [*Friis-Christensen,* 1995]. The data from other near future low-cost satellites will most likely have similar characteristics. Moreover, all POGO data are scalar.

The potential is relatively simple to work compared to the scalar anomalies. For example, the downward continuation of a scalar magnetic anomaly map on a global scale requires simultaneous determination of all of the spherical harmonic coefficients. This is because the variations in the core field direction couple together all the harmonics of the scalar anomalies. However, the harmonics of the potential are decoupled, and the downward continuation of a magnetic potential map is a straightforward procedure. Through the downward continuation of the potential map, we also derive the downward continued satellite magnetic anomaly maps which are very useful for levelling low-altitude aeromagnetic and marine magnetic anomaly maps compiled on a large regional scale. The other goal of this paper is to present the relationship between the magnetic potential and the magnetic susceptibility contrasts of the lithosphere on a global scale. A magnetic susceptibility contrast map displays the basic magnetic characteristics of the lithosphere, which is useful for geological interpretation.

The inversion technique is applied to the satellite magnetic anomaly map shown in Figure 1, and the potential and magnetic susceptibility contrast maps of the lithosphere specified by spherical harmonics of degree 15-60 are determined. A brief geological interpretation of the magnetic susceptibility contrasts is also presented.

Remanent Magnetization Direction of the Oceanic Lithosphere

Based on a global age map of the oceanic lithosphere derived from a self-consistent model of relative plate motions for the last 200 m.y. [*Mueller et al.,* 1994], we compute the remanent magnetization direction of the oceanic lithosphere. The global plate motion model is represented by a set of finite rotation poles and angles which describe relative motion of pairs of adjacent plates at time intervals of about 10 m.y. [*Royer et al.,* 1992]. We build digital maps of the plate and paleoplate distribution (we call paleoplate an area which is now part of a given plate but was attached to another plate, or behaved as an independent plate at some time of its history) and use the age map to derive a map of time intervals corresponding to the kinematic model. The finite rotation parameters are then combined to obtain the motion of each plate with respect to Africa. Combination of this motion with the paleomagnetic poles given by the apparent polar wandering for Africa [*Ziegler et al.,* 1983; *Beck,* 1994] describes the plate motion with respect to the geomagnetic reference frame. The resulting digital maps and the plate motion parameters are used to compute paleolatitude and paleodeclination at $0.5° \times 0.5°$ grid intervals. The paleolatitude at a given point is obtained by rotating the

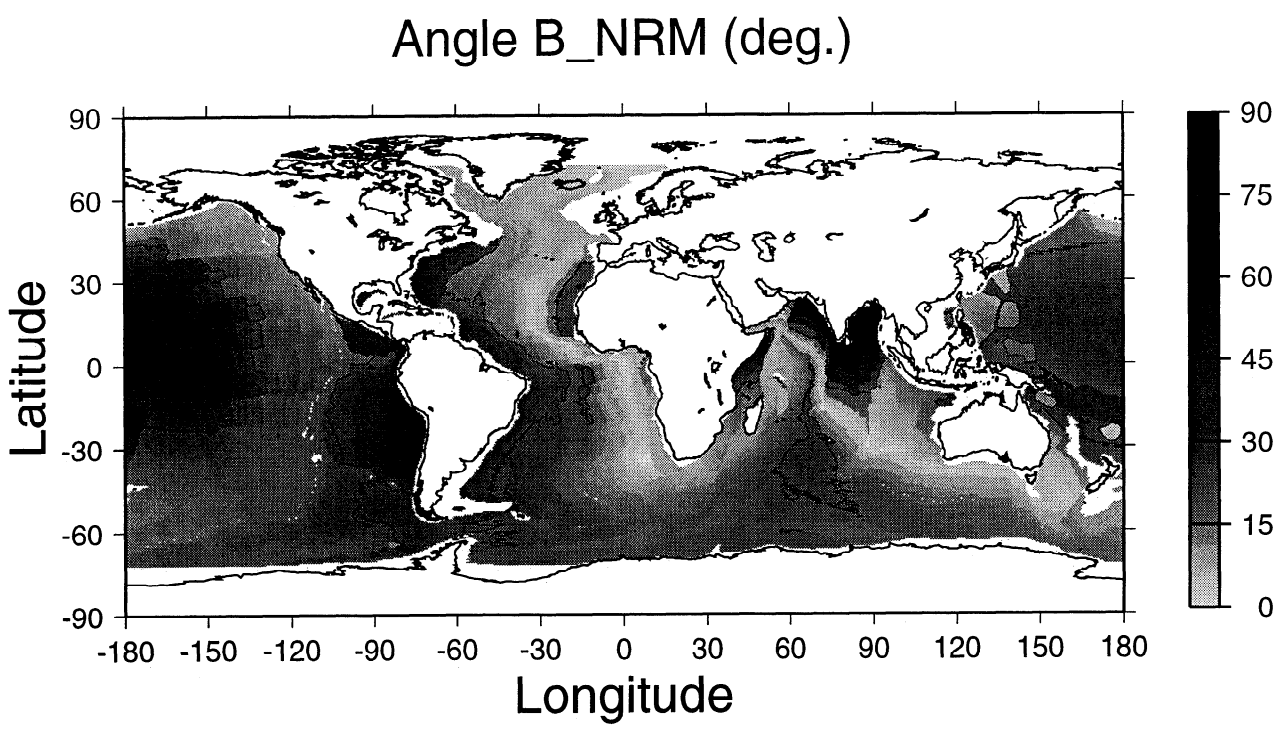

Figure 2. Angle between modeled natural remanent magnetization vectors and the present-day geomagnetic field in oceanic areas. Solid lines show angles of 20°and 45°. Most areas display angles lesser than 20°, and only the oceanic area south of India display angles higher than 45°.

point backward in time and computing the paleoinclination based on a dipolar core field model. By rotating this point and a point immediately north of it from their past positions to their present locations, we determine the paleodeclination as the azimuth of the rotated segment. The paleoposition of Pacific plate prior to 100 Ma is poorly known. It is assumed fixed with respect to other plates, a hypothesis which makes the resulting paleoinclination and paleodeclination of the area less reliable. Figure 2 shows the angle between the core field model GSFC12/83 [*Langel and Estes,* 1985] and the NRM vector thus obtained. The angle is usually less than 20°, sometimes between 20°and 45°(central Pacific Ocean, easternmost Pacific Ocean off South America, westernmost North Atlantic Ocean off North America), and exceptionally higher than 45°in a very limited region near India, which has substantially moved northward within the last 100 m.y. [see *Plates Project,* 1993].

The lack of consistent magnetic anomaly at satellite altitudes associated with the ocean-continent boundary, especially where the seafloor spreading anomalies are short-wavelength features, is probably due to the fact that major part of the anomaly overlaps the core field and thus is removed through the removal of the core field model from the observed data. It also implies that the induced magnetization of the oceanic lithosphere that may give rise to the magnetic anomalies specified by the spherical harmonics of degree greater than 14, with wavelengths shorter than those of the core field, is comparable to the corresponding induced magnetization of the continental crust. The induced magnetization of normal oceanic lithosphere does not produce a significant magnetic anomaly over the areas far from the continents, because it has a horizontally uniform, vertically integrated induced magnetization. The NRM of the KQZ of the North Atlantic produces a magnetic anomaly less than 6 nT at Magsat altitude, similar to low- to medium-amplitude anomalies over the continents. This indicates that the vertically integrated NRM of the oceanic lithosphere is comparable to the vertically integrated induced magnetization of the continental crust and thus to that of the oceanic lithosphere. Therefore the actual direction of the vertically averaged magnetization of the oceanic lithosphere, NRM plus induced, is most likely close to the mean of the direction of the NRM seen in Figure 2 and the direction of the present core field. In other words, the angle between the vertically averaged magnetization of the oceanic lithosphere and the geomagnetic field is about one half that seen in Figure 2. For example, in the Bay of Bengal the vertically integrated magnetization of the oceanic lithosphere makes an angle of about 45°, rather than about 90°, with the present core field direction. We therefore interpret with caution the result of the inversion in the oceanic area located near India and to some extent those from the central and easternmost Pacific Ocean and westernmost North Atlantic Ocean. In other oceanic areas the vertically integrated magnetization direction and geomagnetic field vector can reasonably be considered as collinear.

Inversion Theory

Here we derive the inversion formulas which transform a global scalar magnetic anomaly map into a global magnetic potential map and subsequently into a global magnetic susceptibility contrast map of the lithosphere in a varying core field under the assumption that the magnetization is in the direction of the core field. The geomagnetic coordinate system is adopted throughout this inversion technique. Let V be the magnetic potential of the lithosphere at an observation point $\mathbf{r}$, and $\mathbf{b}$ denote the unit vector in the core field direction at that point. The scalar magnetic anomaly T is defined by

$$T = -\mathbf{b} \cdot \nabla V. \tag{1}$$

Let $\mathbf{b}_1$ be the unit vector along the dipole component of the core field,

$$\mathbf{b}_1 = -\frac{2\cos\theta\hat{\mathbf{r}} + \sin\theta\hat{\boldsymbol{\Theta}}}{\Gamma}, \tag{2}$$

$$\Gamma = \left(1 + 3\cos^2\theta\right)^{1/2},$$

and write

$$\mathbf{b} = \mathbf{b}_1 + \delta\mathbf{b}, \tag{3}$$

where $\hat{\mathbf{r}}$ and $\hat{\boldsymbol{\Theta}}$ are the unit vectors in radial r and colatitude θ directions, respectively, and the vector $\delta\mathbf{b}$ denotes the deviation of $\mathbf{b}$ from $\mathbf{b}_1$ because of the nondipole part of the field. Also, let

$$\tau = \Gamma\, T, \tag{4}$$

$$A = \Gamma\, \delta\mathbf{b} \cdot \nabla V. \tag{5}$$

A is a measure of the contribution to the magnetic anomalies arising from the coupling of the nondipole part of the core field with the magnetic potential of the lithosphere. Now expand V, τ, and A in terms of spherical harmonics as

$$V = a\sum_{n=1}^{N}\left(\frac{a}{r}\right)^{n+1}\sum_{m=0}^{n}\left(V_{nm}^{e}\cos m\phi + V_{nm}^{o}\sin m\phi\right)P_n^m(\cos\theta), \tag{6}$$

$$\tau = \sum_{n=1}^{N}\sum_{m=0}^{n}\left(\tau_{nm}^{e}\cos m\phi + \tau_{nm}^{o}\sin m\phi\right)P_n^m(\cos\theta), \tag{7}$$

$$A = \sum_{n=1}^{N}\sum_{m=0}^{n}\left(A_{nm}^{e}\cos m\phi + A_{nm}^{o}\sin m\phi\right)P_n^m(\cos\theta), \tag{8}$$

in which a is the mean radius of Earth (= 6370 km), r is the radial distance from Earth's center to the observation point, $P_n^m(\cos\theta)$ is the Schmidt normalized associated Legendre function, and N denotes the degree of the highest harmonic included. V_{nm}^{e}, V_{nm}^{o}, τ_{nm}^{e}, τ_{nm}^{o}, A_{nm}^{e} and A_{nm}^{o} are the coefficients of the even (superscript e) and odd (superscript o) spherical harmonic expansions of V, τ and A, respectively. Putting (3)-(8) into (1) yields

$$\tau_{nm}^{e} + A_{nm}^{e} = \xi_{nm}V_{n+1,m}^{e} + \zeta_{nm}V_{n-1,m}^{e}, \tag{9a}$$

$$\tau_{nm}^{o} + A_{nm}^{o} = \xi_{nm}V_{n+1,m}^{o} + \zeta_{nm}V_{n-1,m}^{o}, \tag{9b}$$

in which

$$\xi_{nm} = -\left(\frac{a}{r}\right)^{n+3}\frac{3(n+2)\left[(n+1)^2 - m^2\right]^{1/2}}{2n+3}, \tag{10a}$$

$$\zeta_{nm} = -\left(\frac{a}{r}\right)^{n+1}\frac{(n+1)\left(n^2 - m^2\right)^{1/2}}{2n-1}. \tag{10b}$$

Equations (5), (9a) and (9b) are coupled. They are solved iteratively to determine the magnetic potential V using the observed magnetic anomaly T. Equations (9a) and (9b) are first solved for the spherical harmonic coefficients of the magnetic potential, V_{nm}^{e} and V_{nm}^{o}, by putting A to zero. The resulting magnetic potential is used in (5) to determine the first estimate of A (see Appendix A for details). Using this first estimate, we again solve (9a) and (9b) for V_{nm}^{e} and V_{nm}^{o} and continue this iteration scheme to obtain convergence. Note that no simplifying assumption is made in deriving the above equations and the determination of the magnetic potential is robust, aside from the fundamental nonuniqueness of the solution of (1) (see Appendix B).

The next step is to calculate the magnetic susceptibility contrasts in the lithosphere from the magnetic potential thus obtained. Let $\sigma'(r_o)$ denote the magnetic susceptibility of a volume element dv_o located at the point $\mathbf{r}_o$ in the lithosphere, then the induced magnetization of the volume element $\mathbf{M}(\mathbf{r}_o)$ is

$$\mathbf{M}(\mathbf{r}_o) = \frac{1}{\mu_o}\sigma'(\mathbf{r}_o)\mathbf{B}'(\mathbf{r}_o)dv_o \tag{11}$$

in which $\mathbf{B}'(\mathbf{r}_o)$ is the core field at that point and μ_o is the magnetic permeability. The magnetic potential at an observation point $\mathbf{r}$ is defined by

$$V(\mathbf{r}) = \frac{\mu_o}{4\pi}\int \mathbf{M}(\mathbf{r}_o)\cdot\nabla_o\frac{1}{|\mathbf{r}-\mathbf{r}_o|}dv_o, \tag{12}$$

where the gradient operator ∇_o operates in the $\mathbf{r}_o$ space and integration is over the entire volume of the magnetic sources. The most we can achieve by inverting a magnetic potential map into a magnetic susceptibility contrast map is to determine the lateral variations in the vertically averaged susceptibility of the lithosphere. This is the fundamental nonuniqueness of the inversion of magnetic potential which only yields the vertically integrated magnetic susceptibility contrast (see Appendix B for details). The vertical variations of the magnetic susceptibility cannot be determined through satellite magnetic anomaly maps. Therefore we model the magnetic part of the lithosphere by a magnetic spherical shell of an inner radius R_1 and outer radius a, and as-

sume that its magnetic susceptibility is independent of depth; i.e., we let

$$\sigma'(\mathbf{r}_o) = \sigma(\theta_o, \phi_o) \tag{13}$$

in which σ denotes the vertically averaged magnetic susceptibility contrast of the shell at the colatitude θ_o and east longitude ϕ_o (despite this simplification the solution of (12) is still nonunique; see Appendix B). Similarly, the core field is assumed to be constant with depth within the shell, i.e.,

$$\mathbf{B}'(\mathbf{r}_o) = \mathbf{B}(\theta_o, \phi_o) \tag{14}$$

The core field intensity changes by less than 3% in the upper 50 km of the Earth and its direction hardly changes within this region.

Now decompose $\mathbf{B}$ into dipole part, $\mathbf{B}_1$, and the nondipole part, $\delta\mathbf{B}$,

$$\mathbf{B} = \mathbf{B}_1 + \delta\mathbf{B}, \tag{15}$$

and let W denote the magnetic potential of the shell arising from the magnetization induced by the nondipole part of the core field,

$$W = \frac{1}{4\pi}\int \sigma(\theta_o, \phi_o)\delta\mathbf{B}(\theta_o, \phi_o)\cdot\nabla_o \frac{1}{|\mathbf{r}-\mathbf{r}_o|}dv_o, \tag{16}$$

which is also expanded in terms of spherical harmonics as

$$W = \sum_{n=1}^{N}\frac{a^{n+2}-R_1^{n+2}}{r^{n+1}}\sum_{m=0}^{n}(W_{nm}^e\cos m\phi + W_{nm}^o\sin m\phi)P_n^m(\cos\theta), \tag{17}$$

where W_{nm}^e and W_{nm}^o are the spherical harmonic coefficients of W. Putting (6), (11), and (13)-(17) into (12) and after some algebraic manipulations, we obtain

$$V_{nm}^e - W_{nm}^e = \frac{g_1^o}{n+2}\left[1-\left(\frac{R_1}{a}\right)^{n+2}\right]\left(\gamma_{nm}\sigma_{n+1,m}^e - \gamma_{nm}\sigma_{n-1,m}^e\right), \tag{18a}$$

$$V_{nm}^o - W_{nm}^o = \frac{g_1^o}{n+2}\left[1-\left(\frac{R_1}{a}\right)^{n+2}\right]\left(\gamma_{nm}\sigma_{n+1,m}^o - \gamma_{nm}\sigma_{n-1,m}^o\right), \tag{18b}$$

in which

$$\gamma_{nm} = \frac{3n\left[(n+1)^2-m^2\right]^{1/2}}{(2n+1)(2n+3)}, \tag{19a}$$

$$\delta_{nm} = \frac{(n-1)\left(n^2-m^2\right)^{1/2}}{(2n+1)(2n-1)}, \tag{19b}$$

$\sigma_{n,m}^e$ and $\sigma_{n,m}^o$ are the spherical harmonic coefficients of σ and g_1^o is the coefficient of the dipole term of the core field. Equations (16), (18a), and (18b) are coupled. They are solved iteratively to obtain the spherical harmonic coefficients of the magnetic susceptibility contrasts (see Appendix A for details).

Results

This section presents the resulting magnetic potential and magnetic susceptibility contrasts of the lithosphere. The inversion from a global scalar magnetic anomaly map into a magnetic potential map is nonunique. The solution of the homogeneous equation corresponding to (1) can be added to a given solution without affecting the scalar magnetic anomalies. The homogeneous solution is specified by an infinite series of spherical harmonic functions, similar to *Backus* [1970] series, with a leading term which is a sectorial harmonic, i.e., those with equal degree and order. The sectorial harmonics have constant sign in the north-south direction but change sign in the east-west direction. Being an almost polar orbiter, Magsat passes were almost in the north-south direction and any levelling noise introduced into the scalar data had the potential of exciting the homogeneous solution, and render the inversion of (1) unstable. To suppress the homogeneous solution, *Arkani-Hamed and Strangway* [1985b] applied a directional filter to the scalar map by setting the sectorial harmonic coefficients to zero. We calculate two magnetic potential models, with and without using the directional filter. We also calculate two corresponding magnetic potential models using only the dipole component of the core field for comparison.

Magnetic Potential

The magnetic anomalies seen in Figure 1 are transferred to the geomagnetic coordinate system, multiplied by the Γ factor (see equation (4)) and then expressed in terms of spherical harmonics (the results will be shown in the geographic coordinate system for easy correlation with geological features). Using the harmonic coefficients of the magnetic anomalies and the core field model of 1980 [*Langel and Estes*, 1985], the spherical harmonic coefficients of the magnetic potential are determined by (5), (9a), and (9b). Convergence of the iterations is monitored by calculating the difference between magnetic potentials of successive iterations. Figure 3a shows the magnetic potential model obtained after 5 iterations which incorporates the entire core field model and uses the directional filter, and Figure 3b shows the difference between the magnetic potentials of iterations 5 and 4. Figure 3b is dominated by high-frequency, low-amplitude features with amplitudes well below 0.03 nT m everywhere, except in central Africa and the nearby Atlantic Ocean where the amplitudes are below 0.15 nT m, which are still less than 7% of the prominent magnetic potential signals in that area. Figure 3c shows the power spectra of the differences between the magnetic potentials of successive iterations. A power spectrum, W_n, is calculated through

$$W_n = \frac{\sum_{m=0}^{n}\left(C_{nm}^2 + S_{nm}^2\right)}{2n+1} \tag{20}$$

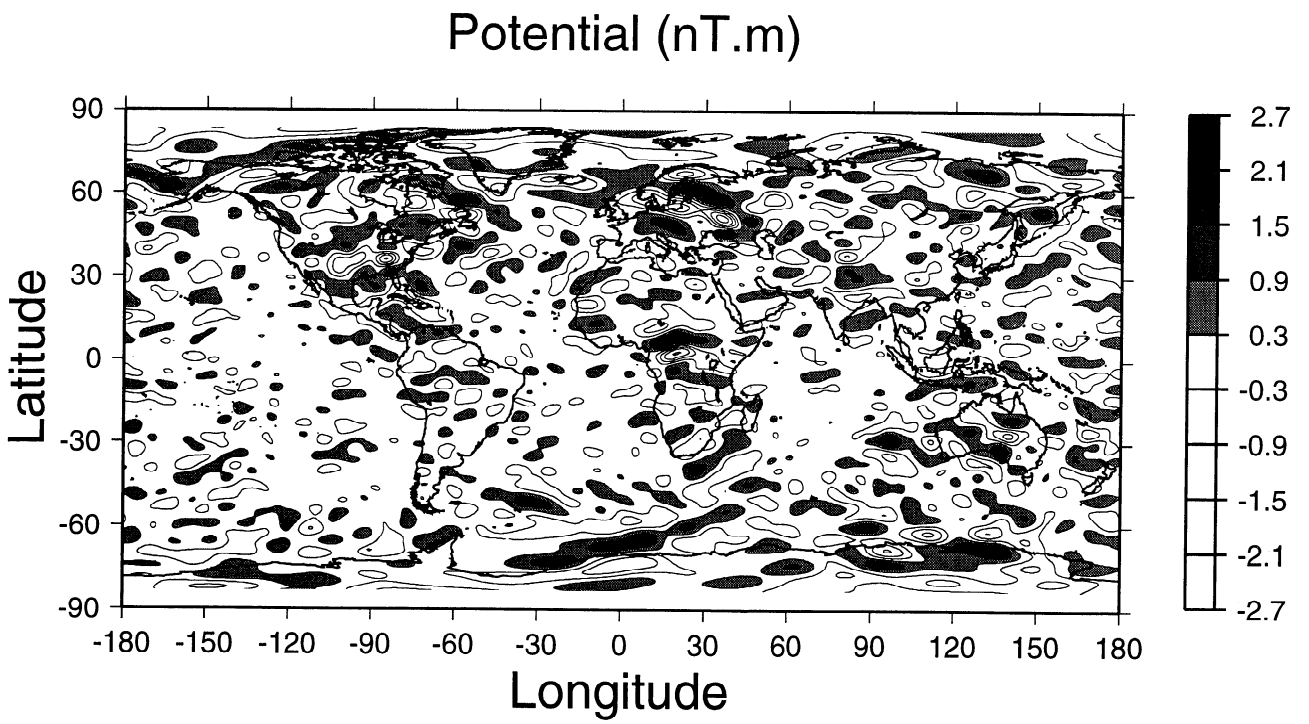

Figure 3a. Magnetic potential of Earth at 400 km altitude computed from the scalar magnetic anomaly displayed in Figure 1.

where C_{nm} and S_{nm} stand for the coefficients of the even and odd harmonics of the potential differences. Figure 3c confirms that the iteration solution did essentially converge, and the magnetic anomalies seen in Figure 1 are converted to the magnetic potential of their source bodies as seen in Figure 3a. The fast and stable convergence of the iteration is largely due to the fact that (1) is linear.

Figure 4a shows the degree correlation coefficients, η_n, among the four potential models obtained using the

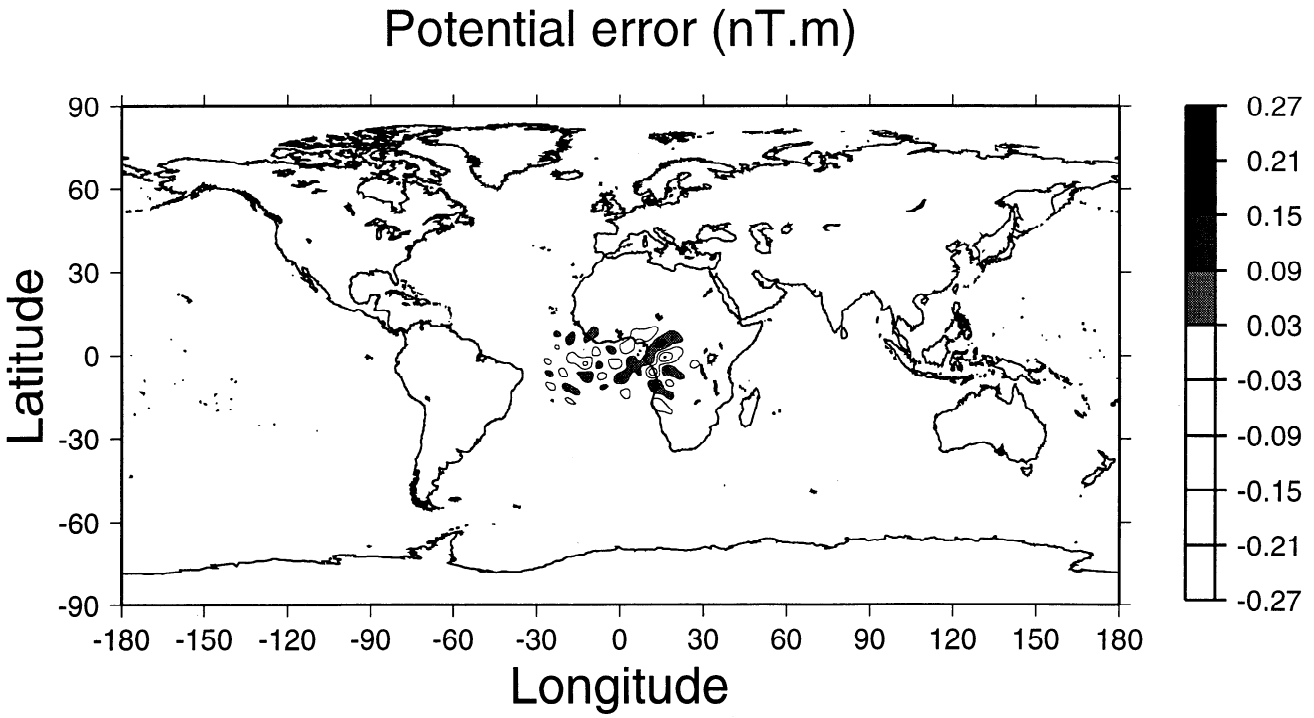

Figure 3b. Difference between the magnetic potential of Earth at 400 km altitude after 5 and 4 iterations. Notice that the scale is an order of magnitude smaller than for Figure 3a.

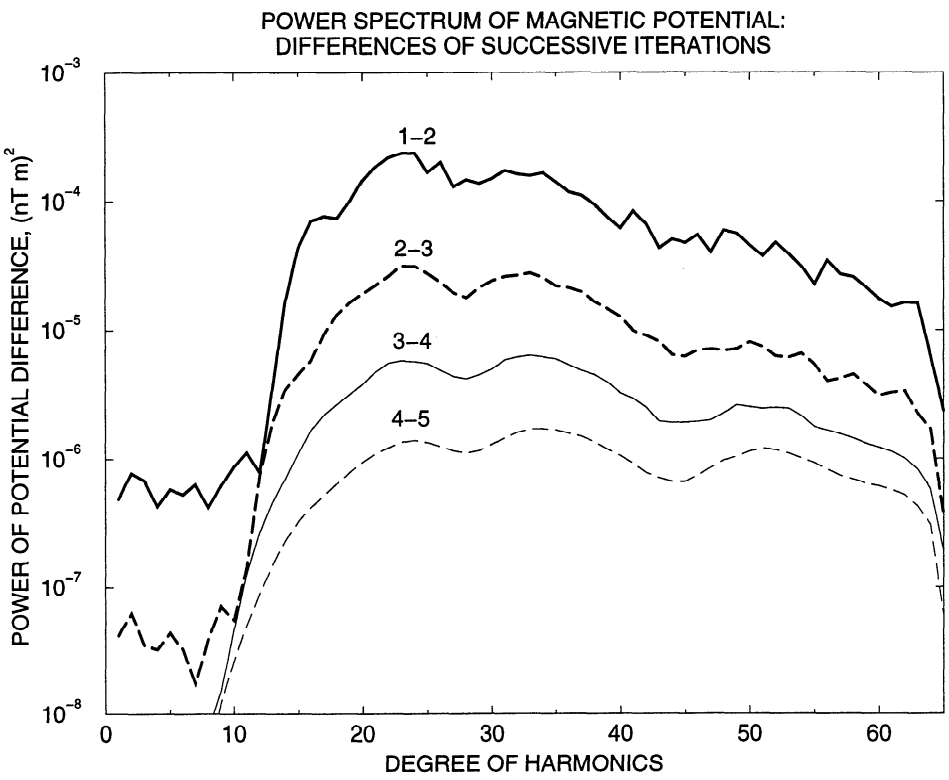

Figure 3c. Power spectra of the difference of the potential between two successive iterations. The numbers on the curves denote the iteration. The improvement of the fifth iteration is minor and the procedure has converged.

entire core field or the dipole component of the core field and with or without directional filtering the scalar magnetic anomaly map. The correlation coefficient is defined as

$$\eta_n = \frac{\sum_{m=0}^{n} (C_{nm}C'_{nm} + S_{nm}S'_{nm})}{[\sum_{m=0}^{n} (C_{nm}^2 + S_{nm}^2) \sum_{m=0}^{n} (C_{nm}'^2 + S_{nm}'^2)]^{1/2}} \quad (21)$$

where (C_{nm}, S_{nm}) and (C'_{nm}, S'_{nm}) stand for the spherical harmonic coefficients of a pair of potential models. The models correlate strongly on a global basis; the correlation coefficients are greater than 0.94 and usually greater than 0.97, emphasizing that the directional filtering and the nondipole components of the core field have minor effects on the resulting magnetic potential on a global scale. The minor effect of the directional filtering, contrary to what was observed by *Arkani-Hamed and Strangway* [1985b], is largely due to the fact that the stringent scalar magnetic anomaly map used in the present studies is less contaminated by nonlithospheric sources than the map used by Arkani-Hamed and Strangway. The stringent map is based on more recent Magsat maps produced by *Ravat et al.* [1995], who removed long-wavelength along-track variations that trend almost north-south near the equator and thereby reduced the amplitude of those harmonics which can excite the sectorial harmonics of the potential in the inversion process. The minor effect of the non dipole components is expected because the core field direction significantly differs from the direction of its dipole component in only a few regions. Nevertheless, because of the dominance of the dipole component of the core field and the small possibility that it will tend to enhance the potential through the inversion routine, we prefer the magnetic potential model derived using the entire core field and the directional filter and will use this model hereafter.

There is a good correlation over well-defined features of our magnetic potential map and the ΔZ component maps published by *Cain et al.* [1989], *Cohen and Achache* [1990], and *Ravat et al.* [1995]. However, small-scale, low-amplitude features are different; they are more likely affected by the noise in the original data and the data processing noise. For a quantitative comparison, we determine the degree correlation coefficients between our potential and that of Cain et al. (the harmonic coefficients up to degree 49 were provided by J. Cain as the preferred model). The degree correlation coefficients (Figure 4b) are usually higher than 0.5 for harmonics of degree 16-38 but decrease for higher degree harmonics. We also calculate the ΔZ component from our potential model using

$$\Delta Z = -\hat{\mathbf{r}} \cdot \nabla V, \quad (22)$$

and correlate them with the ΔZ component maps derived by *Cohen and Achache* [1990] and *Ravat et al.* [1995]. *Cohen and Achache's* [1990] map was provided

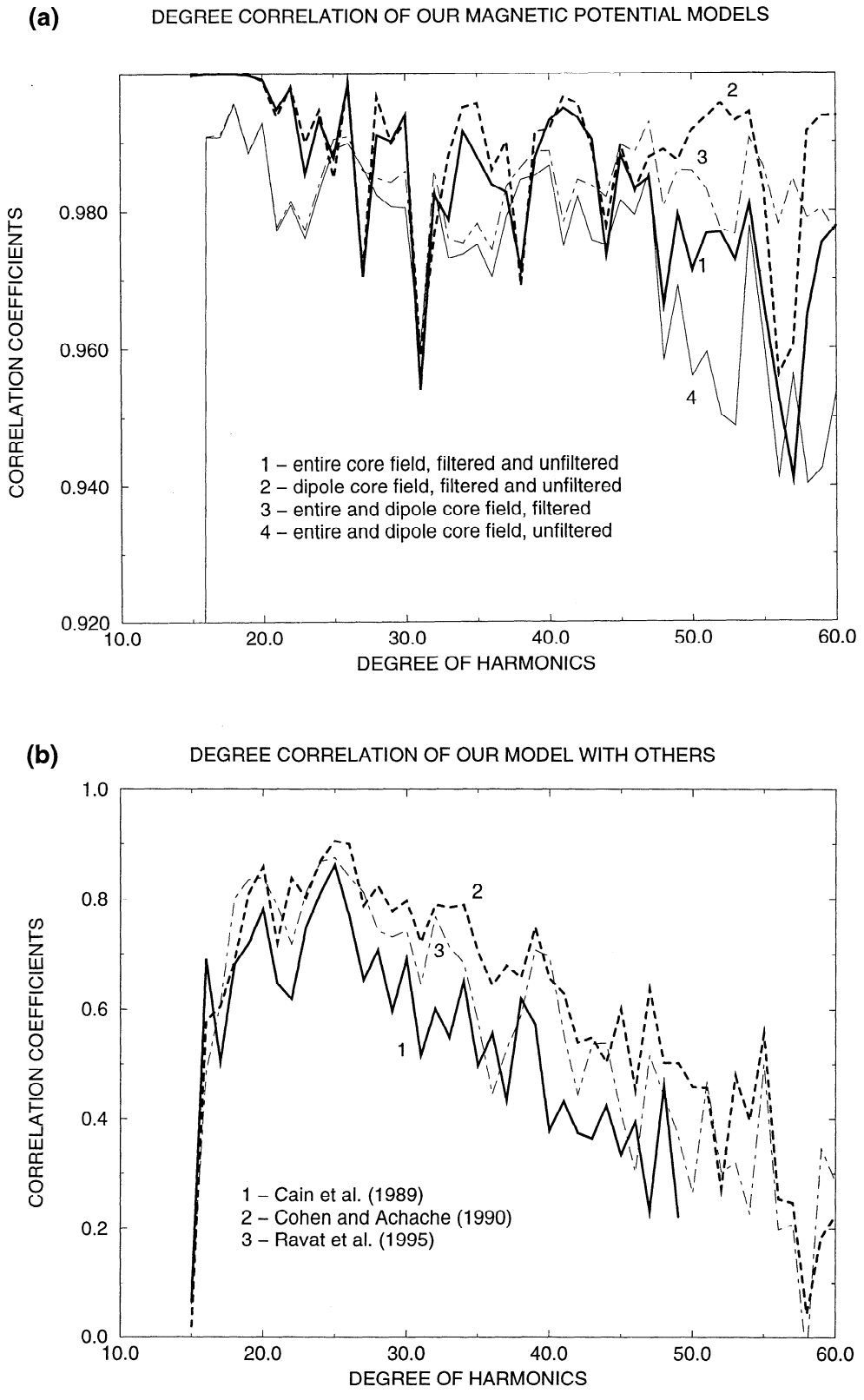

Figure 4. Degree correlation coefficients among different data sets (a) among the magnetic potential models calculated in this paper, (b) between our preferred magnetic potential model and that of *Cain et al.* [1989], and between the ΔZ component calculated from our potential model and the ΔZ component maps of *Cohen and Achache* [1990], and *Ravat et al.* [1995], and (c) between the ΔZ component maps of Cain et al., Cohen and Achache, and Ravat et al.

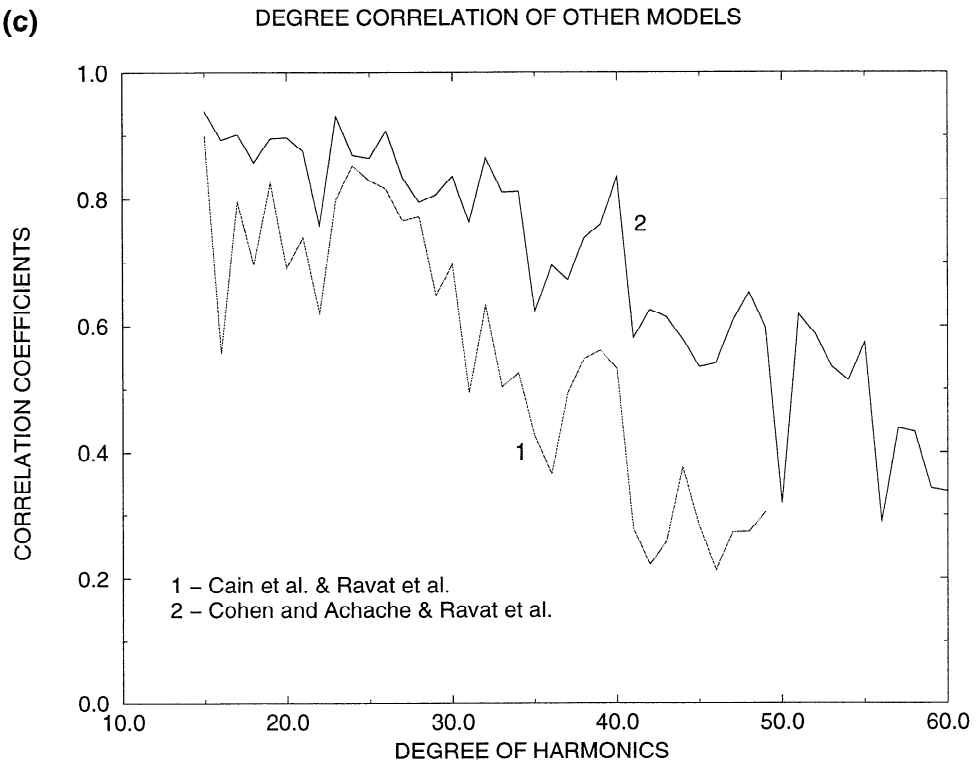

Figure 4. (continued)

on a $2^\circ \times 2^\circ$ grid between $\pm 60^\circ$ latitudes covering about 87% of the globe (Y. Cohen, personal communication, 1995). To determine the spherical harmonic coefficients of this map, we first produce a composite global map by covering the remaining 13% of the globe as follows: the polar regions north of 60° latitude and south of -60° latitude are filled using Ravat et al.'s data; in the region between 55° and 60° north and between -55° and -60° south, Cohen and Achache's map is tapered to zero poleward and Ravat et al.'s map is tapered to zero equatorward using the Hanning function, and the results are added. In the region between $\pm 55^\circ$ latitudes Cohen and Achache's map is used. Ravat et al. presented their ΔZ component for the whole globe, we use the spherical harmonic coefficients of their map (M. Purucker, personal communication, 1995). Included in Figure 4b are the degree correlation coefficients between these maps and ours. Figure 4c shows the degree correlation between the ΔZ components of Ravat et al. and Cain et al. and Ravat et al. and Cohen and Achache for comparison. In general, there is a consistent correlation among these four different maps: Cain et al.'s, Cohen and Achache's, Ravat et al.'s, and ours. Our magnetic potential model somewhat better correlates with Cohen and Achache's and Ravat et al.'s maps. The correlation coefficients are usually higher than 0.5 for harmonics of degree up to 40, but they decrease for higher-degree harmonics.

Downward Continued Magnetic Anomalies

Following the compilation of the magnetic anomaly map of North America by *Hinze et al.* [1988] as part of the Decade of North American Geology (DNAG), aeromagnetic and marine magnetic anomaly maps are being compiled over Africa, South America, Asia, North Atlantic Ocean, and Arctic Ocean. These maps are compiled by merging many surveys covering small areas. However, the comparison of the upward continued magnetic anomalies of North America with the satellite magnetic anomalies derived from Magsat data demonstrated that the compilation process of the North American map had introduced significant error into the intermediate scale magnetic anomalies [*Arkani-Hamed and Hinze,* 1990], as subsequently confirmed by *Grauch* [1993] using a completely independent procedure. Therefore a downward continued satellite map is useful for levelling the low-altitude aeromagnetic and marine magnetic surveys.

Downward continuation of a satellite scalar magnetic anomaly map over a small area is a linear operator in the Fourier domain; each Fourier coefficient of the anomalies is multiplied by a respective geometrical factor. This is because the core field direction can safely be assumed constant over the area. However, because of significant variations of the core field direction over the globe the downward continuation of a global scalar magnetic anomaly map requires simultaneous determination of all of the spherical harmonic coefficients due to their strong coupling. Equations (9a) and (9b) show that the laterally varying core field direction couples together different harmonics of the magnetic potential in order to give rise to a given harmonic of the scalar magnetic anomaly. Unlike for a scalar magnetic anomaly map, the downward continuation of a global magnetic potential map in the spherical harmonic domain is straight forward, as seen from (6). A spherical harmonic co-

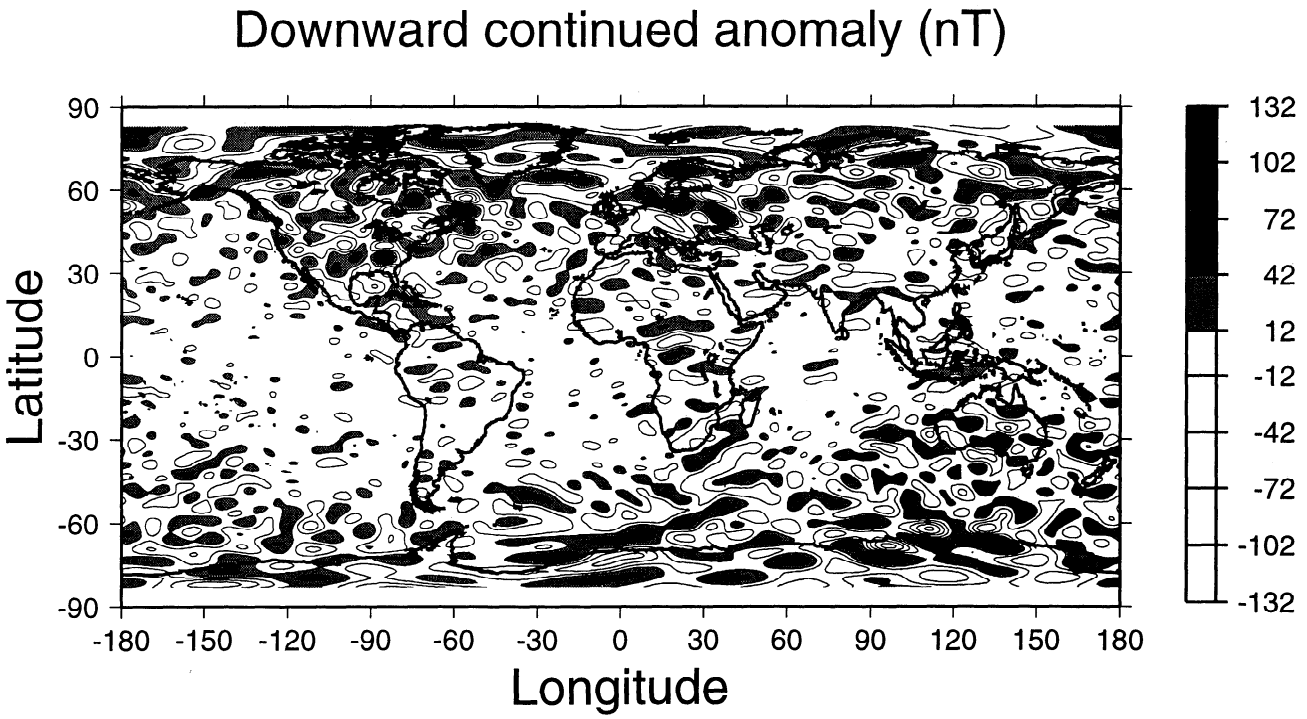

Figure 5. Scalar magnetic anomaly of Earth downward continued to 10 km altitude from the scalar magnetic anomaly displayed in Figure 1.

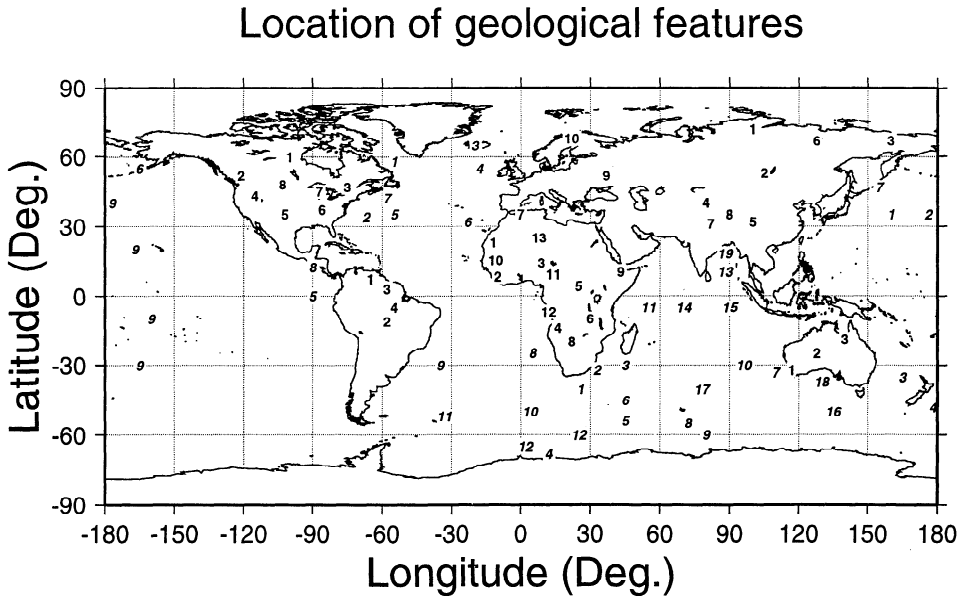

Figure 6. Location of various features referred to in the text. Numbers are normal for continents (Africa, North America, South America, Australia, and Eurasia) and italic for oceans (Atlantic, Indian, Pacific). See Table 1 for the approximate latitudes and longitudes at the center of each feature.

Table 1. Locations of Geological Features With Well-Defined Magnetic Signatures

Number	Geological Feature	Longitude	Latitude
	Africa		
1	Mauritanian Craton	348	23
2	Liberian Craton	350	8
3	Nigerian Craton	9	14
4	Angolan Craton	16	-14
5	Central African Craton (Bangui Anomaly)	25	4
6	Zambian Craton	30	-10
7	Atlas Mountains	0	35
8	South African Mobile Belt	20	-15
9	Afar Rift	43	10
10	Cassamance Aulacogen	349	15
11	Benue-Cameroonland Aulacogen	14	9
12	Luanda Aulacogen	12	-7
13	Ahaggar	8	25
	North America		
1	Canadian Shield	260	60
2	Rockies Mountains	239	52
3	Grenville/Superior Boundary	285	47
4	Basin and Range	245	43
5	Anadarko Basin	258	35
6	Kentuky anomaly	274	37
7	Michigan Basin	273	45
8	Willingston Basin	257	48
	South America		
1	Guiana Craton	295	7
2	Central Brazilian Craton	302	-11
3	Takutu Aulacogen	302	3
4	Amazon Aulacogen	305	-5
	Australia		
1	Yilgarn Craton	117	-32
2	Musgrave Craton	128	-25
3	Mount Isu Craton	140	-19
	Eurasia		
1	Anabar Craton	100	72
2	Alden Craton	105	53
3	Omolon Craton	160	67
4	Tarim Craton	80	40
5	Yangche Craton	100	32
6	Verkhoiansk Mountains	128	67
7	Himalaya Mountains	82	31
8	Tibet Plateau	90	35
9	Kursk Anomaly	37	52
10	Baltic Craton	22	68
	Atlantic Ocean		
1	Labrador Sea	305	58
2	Bermuda Rise	293	34
3	Iceland	340	65
4	Rockall Plateau	342	55
5	Western Atlantic KQZ	305	35
6	Eastern Atlantic KQZ	337	32
7	Nova Scotia Basin	302	42
8	Walvis Ridge	5	-25
9	Rio Grande Rise	325	-30
10	Meteor Rise	4	-50
11	KQZ off Falkland Plateau	327	-52

Table 1. (continued)

Number	Geological Feature	Longitude	Latitude
	Indian Ocean		
1	Agulhas Plateau + KQZ	26	-40
2	Mozambique Plateau + KQZ	33	-32
3	Madagascar Plateau + KQZ	45	-30
4	Maud rise + KQZ	12	-68
5	Conrad Rise + KQZ	45	-54
6	Crozet-Del Cano Rise	45	-45
7	Naturaliste Plateau	110	-33
8	Northern Kerguelen Plateau	72	-55
9	Southern Kerguelen Plateau	80	-60
10	Broken Ridge	96	-30
11	Seychelles Plateau	55	-5
12	KQZ off Antarctica	2	-65
12	KQZ off Antarctica	25	-60
13	KQZ off India	88	10
14	Chagos-Laccadives Ridge	70	-5
15	Ninetyeast Ridge	90	-5
16	Australian-Antarctic Discordance (area A)	135	-50
17	Amsterdam-Saint Paul Islands	78	-40
18	Great Australian Bight	130	-37
19	Bengal Basin	88	18
	Pacific Ocean		
1	Shatsky Rise	160	35
2	Hess Rise	176	35
3	Lord Howe Rise	165	-35
4	Campbell Plateau	178	-48
5	Galapagos Ridge	270	0
6	Aleutian Subduction Zone	195	55
7	Kouril-Kamtchatka Subduction Zone	155	47
8	Central America Subduction Zone	270	12
9	Central Pacific KQZ	183	40
9	Central Pacific KQZ	193	20
9	Central Pacific KQZ	200	-10
9	Central Pacific KQZ	195	-30

efficient of degree n is multiplied by $(r_1/r_2)^{n+1}$ in order to downward continue the potential from r_1 to r_2. We downward continue the magnetic potential from the satellite altitude of 400 km to the surface of Earth and determine the scalar magnetic anomalies at the surface using (1). Figure 5 shows the resulting downward continued map. The downward continuation increases the amplitude of the anomalies. The enhancement is greater, by more than an order of magnitude, for higher-degree harmonics. Consequently, many broad anomalies at satellite altitude are now separated into two or more small-sized anomalies. For example, the east-west elongated positive anomaly at the satellite altitude over the United States, arising from overlapping of the Anadarko and Kentucky anomalies (see Figure 6 for the geographic location, and Table 1 for the approximate latitude and longitude of the centers of the features, cited in this paper), is clearly separated into two distinct anomalies in the downward continued map. Also, there is no visible magnetic anomaly of Michigan basin at the satellite altitude, whereas a well-defined positive anomaly overlies the basin in the downward continued map. Moreover, downward continuation tends to enhance the east-west elongation of small-scale anomalies (see the oceans, for example). This enhancement more likely arises from the fact that the long-wavelength components of the magnetic anomalies in the north-south direction were suppressed by along-track filtering used in the derivation of the satellite magnetic anomaly map, whereas such filtering was not applied in the east-west direction.

Downward continuation does not overcome the difficulty of directly correlating the scalar magnetic anomalies with their magnetic source bodies. There is no sign change for anomalies at the equator, and there is no significant poleward shift of the midlatitude anomalies. Also, the anomalies near the equator are still much weaker than those at midlatitudes and polar regions.

Magnetic Susceptibility Contrasts

Having obtained the magnetic potential, we next solve (16), (18a), and (18b) for the magnetic susceptibility contrasts in the lithosphere, again by iteration. The magnetic part of the lithosphere is modeled by a spherical shell of thickness 40 km ($R_1 = 6330$ km). The iterations are monitored by calculating the difference between the magnetic susceptibility contrasts of successive iterations. Figure 7a shows the resulting magnetic susceptibility contrasts after 5 iterations, and Figure 7b displays the difference between the magnetic sus-

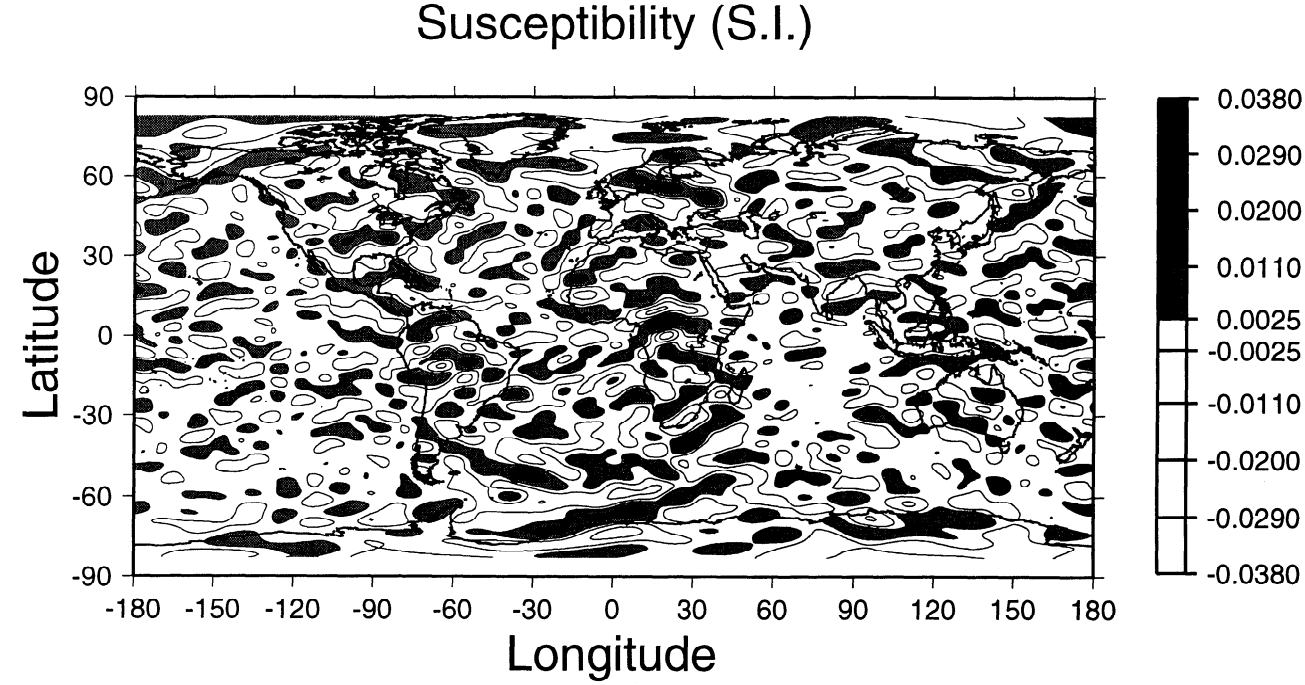

Figure 7a. Magnetic susceptibility contrast of Earth's lithosphere assuming a 40-km-thick magnetic layer computed from the potential displayed in Figure 3a.

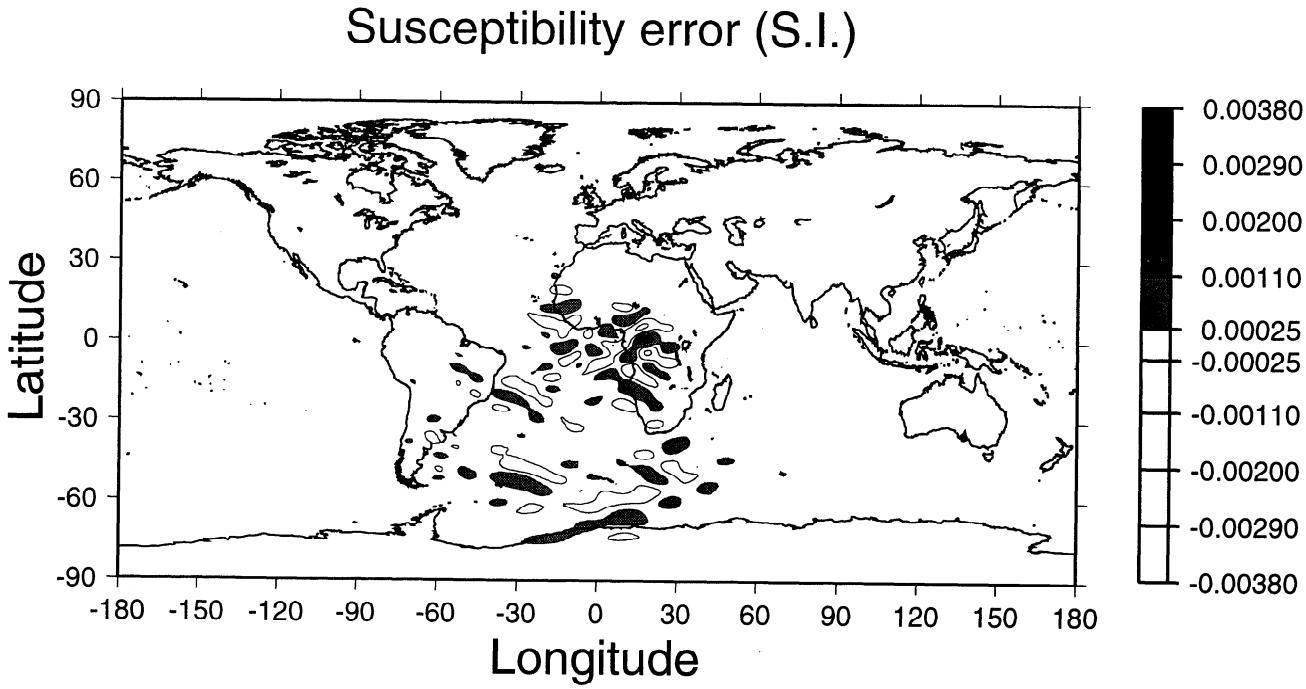

Figure 7b. Difference between the magnetic susceptibility contrasts after 5 and 4 iterations. Notice that the scale is an order of magnitude smaller than for Figure 7a.

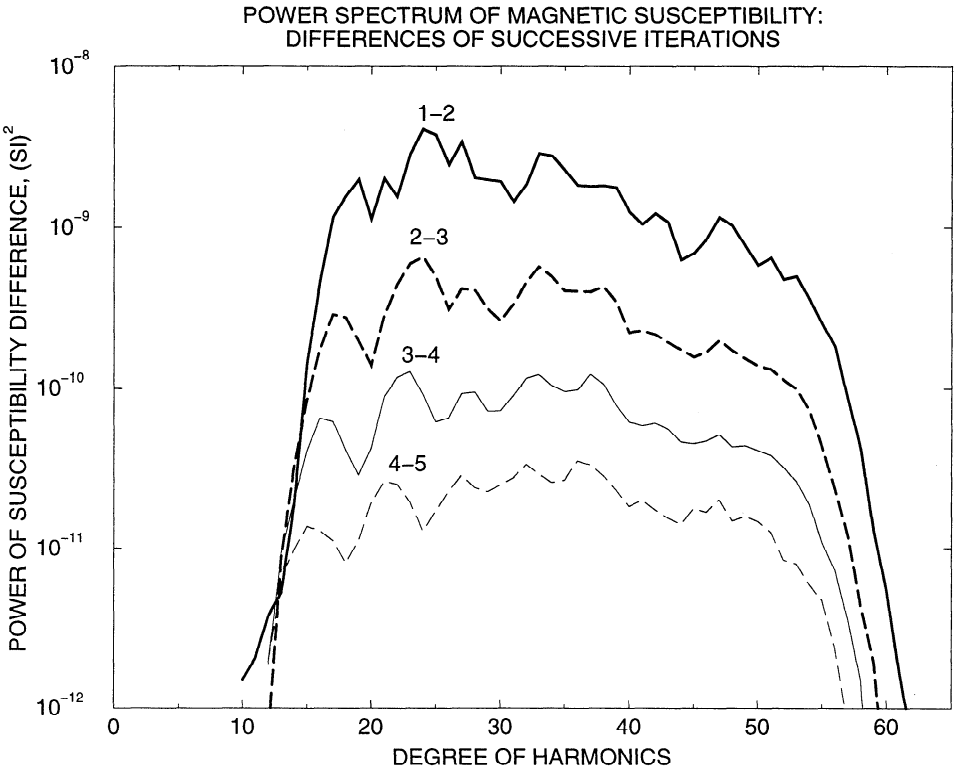

Figure 7c. Power spectra of the difference of the susceptibility between two successive iterations. The numbers on the curves denote the iterations. The improvement of the fifth iteration is minor and the procedure has converged.

ceptibility contrasts of iterations 5 and 4. The power spectra of the differences between the magnetic susceptibility contrasts of subsequent iterations (Figure 7c) emphasize that the iteration converged quite effectively and the major features of the magnetic potential are now converted to those of the magnetic susceptibility contrasts in the lithosphere. Again, the fast and stable convergence of the iteration is because the magnetic potential and magnetic susceptibility are linearly related in (12).

Equations (5), (9a), and (9b) and (16), (18a), and (18b) show that the inversion is not a straightforward operation. Spherical harmonic coefficients of different degrees of the magnetic susceptibility contrasts couple to those of the core field to produce a given spherical harmonic coefficient of the observed magnetic anomalies. All of the harmonic coefficients of the susceptibility contrasts must be determined simultaneously. This is a fundamental characteristic of the inverse process. Moreover, due to the coupling, the resulting susceptibility contrasts contain a wider spectrum of harmonics than the input magnetic anomaly map which consists of harmonics of degree 15-60. The harmonic coefficients of degree less than 15, and those greater than 60, of the magnetic susceptibility contrasts arise solely from the above mentioned coupling. These harmonic coefficients are not reliable, and they are not included in Figure 7a. Major magnetic anomalies associated with the lithospheric magnetization contrasts specified by harmonics of degree less than 15 were already removed from the magnetic anomaly map due to their overlap with the core field, and those specified by harmonics of degree greater than 60 were also removed because of their strong contamination by nonlithospheric sources.

Comparison of Figures 1 and 7a shows the major effects of the inversion. The anomalies near the polar regions have retained their general shape. For example, the positive anomaly over the Kursk iron formation (location 9 in Figure 6) is due to a positively magnetized body. On the other hand, the anomalies in the equatorial region have changed their sign. For example, the well-known negative Bangui anomaly of central Africa (location 11 in Figure 6) arises from a positively magnetized body. The magnetic susceptibility contrasts associated with the magnetic anomalies in the midlatitudes are now shifted poleward with respect to the anomalies. For example, the positive anomaly associated with the Tarim basin in Asia (location 4 in Figure 6) is shifted northward by about 200 km. Moreover, the amplitude of the magnetic anomalies near the poles is significantly greater than those in the equatorial region, whereas the magnetic susceptibility of their source bodies is comparable. This is better illustrated by comparing the magnetic anomalies and magnetic susceptibility contrasts of South America with those of North America. The magnetic anomalies of South America which are located in the geomagnetic equatorial zone are appreciably weaker than those of North America, whereas the magnetic sus-

ceptibility contrasts of the two continents are similar in magnitude. Also, the inversion procedure in effect includes downward continuation. The higher-degree harmonics of the resulting magnetic susceptibility contrast map have enhanced compared to the corresponding harmonics of the magnetic anomaly map at satellite altitudes.

Our susceptibility contrast map correlates with the one published by *Arkani-Hamed and Strangway* [1985b, Figure 12] in which the dipole component of the core field was adopted. This is because the core field is dominated by the dipole component, and therefore the effects of the nondipole parts of the core field are small compared to the dipole part, as illustrated in Figure 4a. Major susceptibility features of continents are similar on both maps, although detailed shapes of the features differ, and small-scale features have appreciable differences. There are, however, significant improvements over oceanic regions. In Arkani-Hamed and Strangway's map there are northwest-southeast trending features in the east Pacific Ocean, west of South America, and a tendency for a northeast-southwest trend in the Indian Ocean, both of which are absent in our map. This is largely due to the more accurate scalar magnetic anomaly map used in the present study.

We study the effects of nondipole components of the core field on the resulting magnetic susceptibility contrasts by comparing the results of inversion using the entire core field and the dipole part of the core field alone. Figure 8 shows the difference between the two magnetic susceptibility contrasts maps. The major differences are in the South Atlantic Ocean and adjacent continents. This is because the nondipole part of the core field is appreciable over this area. Figures 9a and 9b show the magnetic susceptibility contrast maps obtained over this area using the entire core field and the dipole component of the core field, and Figure 9c is the difference between these two maps (Figure 9b minus Figure 9a). The magnetic susceptibility contrasts obtained using the entire core field are significantly greater than those determined using the dipole field alone. The susceptibility contrast of the prominent Bangui anomaly is about a factor of 30 % greater, that of Agulhas Plateau is about 50 %, and the elongated feature off the coast of Antarctica and that associated with Falkland Plateau are about 100 % greater. Although major features seems similar in shape, detailed investigation shows that they are horizontally shifted by as much as about 100 km. This may not have a significant effect on the preliminary interpretation of satellite anomalies, but it may prove to be important for locating the magnetic sources more precisely.

Discussion and Conclusions

The inversion technique developed in this paper in order to transform a global scalar magnetic anomaly map into a global magnetic susceptibility contrasts map consists of two linear but coupled operations. The first operation inverts a scalar magnetic anomaly map into a magnetic potential map, while the second operation transforms the potential map into a magnetic susceptibility contrast map. Each operation is cast into a matrix equation to be solved iteratively. The coupling term related to the dipole part of the core field is retained in the left-hand side, while those related to the nondipole

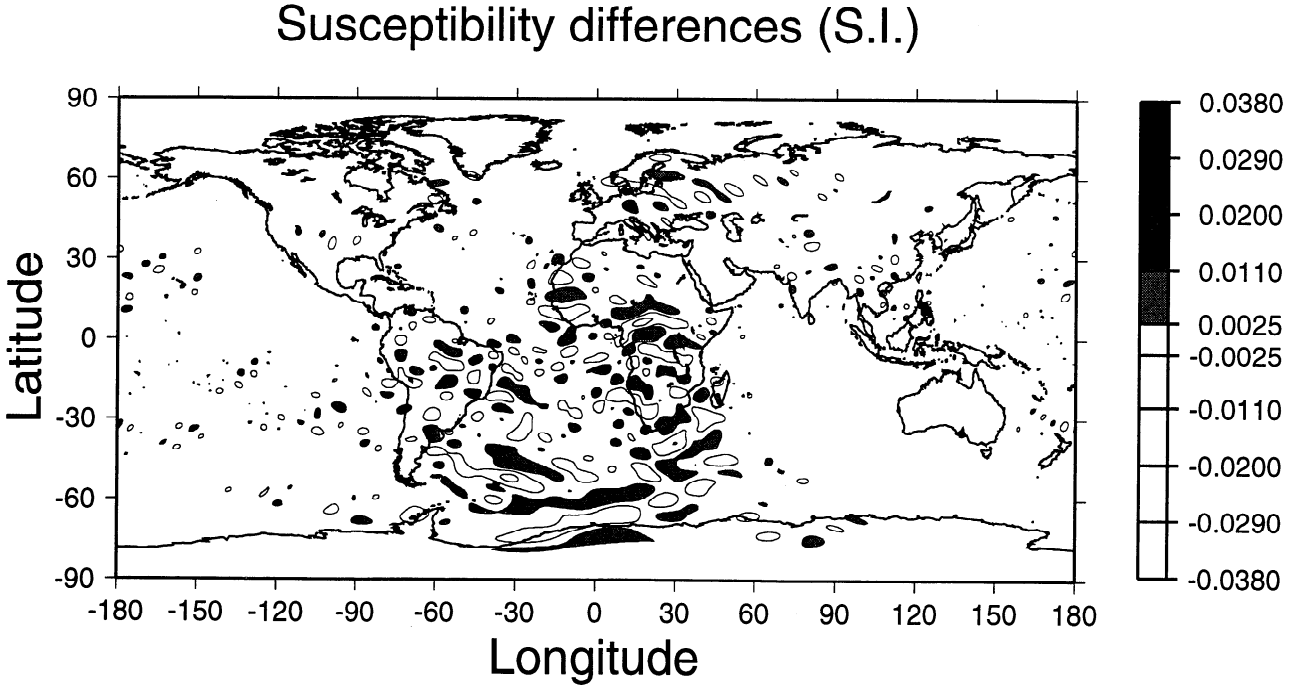

Figure 8. Difference between the magnetic susceptibility contrast models a and b, obtained using the entire core field model and the dipole part of the core field, respectively (i.e., model b minus model a).

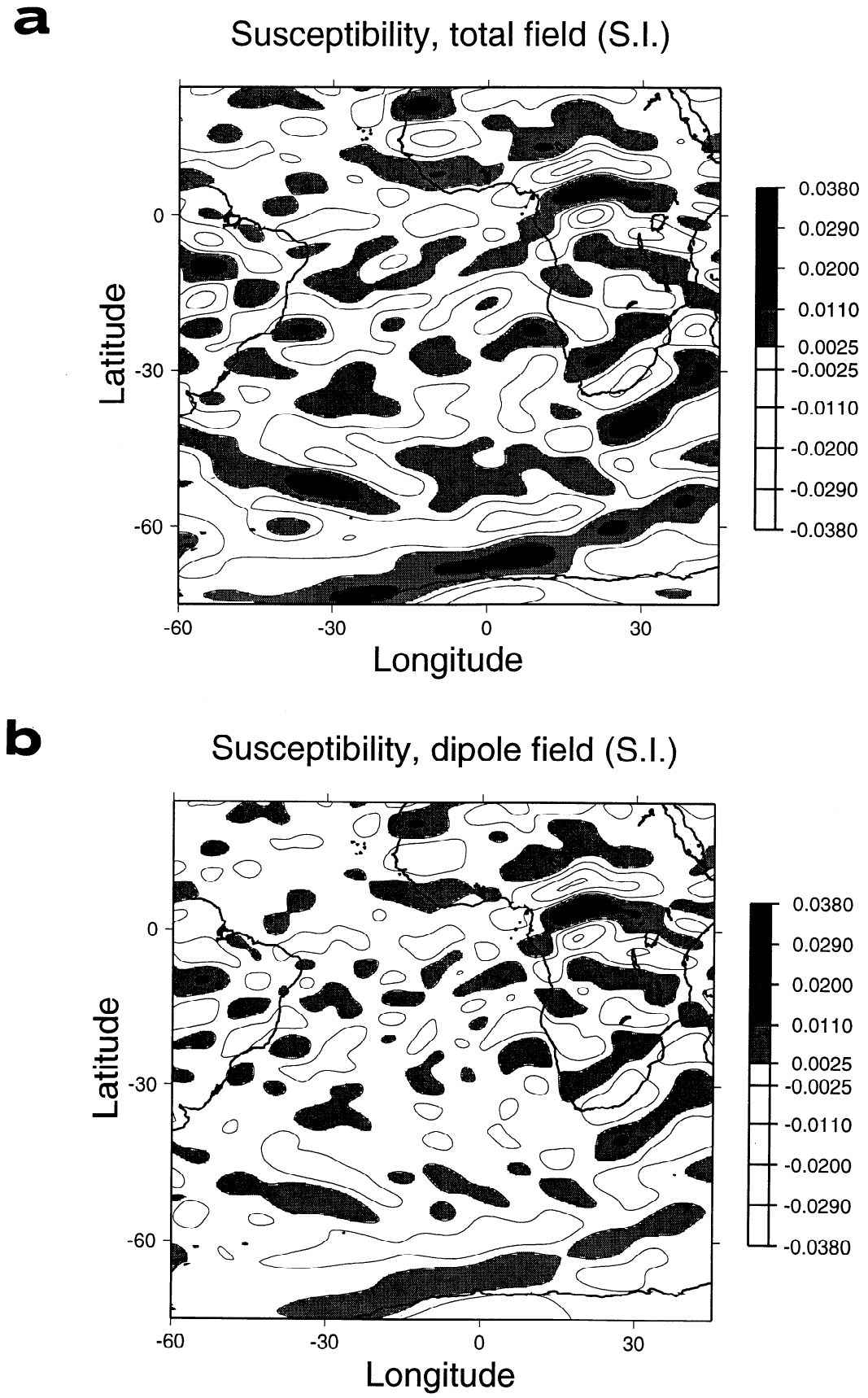

Figure 9. Magnetic susceptibility contrast model determined using (a) the entire core field, and (b) the dipole component of the core field. (c) Difference between these two models, i.e., Figure 9c equals Figure 9b minus Figure 9a.

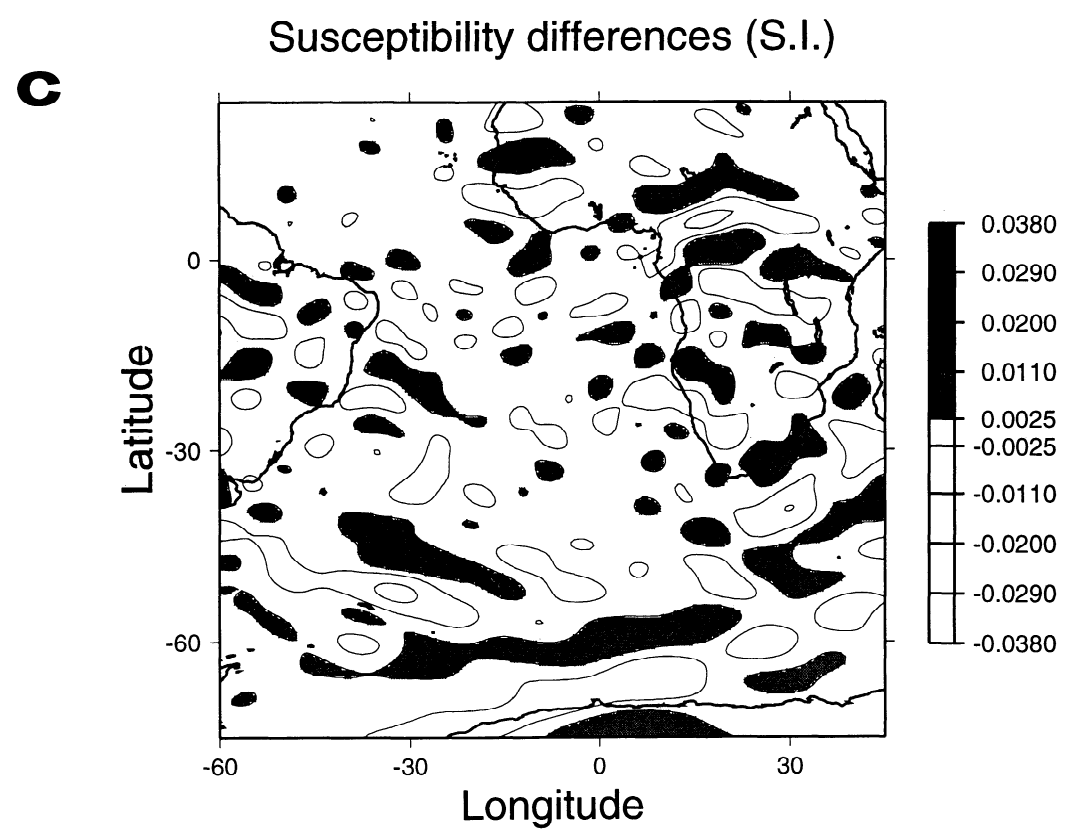

Figure 9. (continued)

parts are kept in the right-hand side of the equations.

The inversion technique was applied to the scalar magnetic anomaly map derived from POGO and Magsat data [*Arkani-Hamed et al.*, 1994]. The resulting magnetic potential map is correlated with the magnetic potential map published by *Cain et al.* [1989], and the ΔZ component map derived from our potential map is correlated with those of *Cohen and Achache* [1990] and *Ravat et al.* [1995]. The susceptibility contrast map alleviates the difficulty encountered in the direct correlation of scalar magnetic anomalies with their source bodies. The features in the equatorial zone of the scalar anomaly map have changed the sign in the susceptibility contrast map, and their amplitudes are enhanced compared to those of features in polar regions. The features in midlatitudes are shifted poleward by different amounts depending on their locations. Moreover, due to the enhancement of higher-degree harmonics compared to lower-degree ones, the broad features in the scalar anomaly map are divided into two or more small size features in the susceptibility contrast map, which better delineate geological formations.

There has been a tremendous effort in the last 20 years, since POGO satellites and more importantly since the Magsat mission, to analyze and interpret the intermediate wavelength satellite magnetic anomalies of Earth in terms of geological features both on global and regional scales [see *Langel et al.*, 1991]. Any interpretation on a global scale will inevitably reiterate many of the interpretations made previously. To minimize the reiteration, we identify major common magnetic characteristics rather than explaining individual anomalies. The regional scale interpretations are naturally better constrained than global ones. This is partly because better data cleaning, especially from external field contributions, is possible on regional scale and partly because geological information is available in many of the regions considered. On the other hand, global scale interpretations enable worldwide comparison of the magnetic sources and thus identify certain geological features with common magnetic characteristics independent of their particular geographic locations, providing means to understand basic characteristics of the magnetic nature of the lithosphere. *Frey* [1982] was probably the first Magsat investigator to provide a list of major geological features of Earth with well-defined magnetic anomalies. However, because of the above mentioned difficulty concerning the direct correlation of magnetic anomalies with their source bodies, he had to list different magnetic signatures under a common geologic category. *Arkani-Hamed and Strangway* [1985b] calculated the lateral variations in the magnetic susceptibility of the lithosphere and thus made direct quantitative correlation of magnetization contrasts with geological features. However, they assumed the magnetization to be in the direction of the dipole component of the core field. Moreover, the global magnetic anomaly map they used was based on Magsat data alone and they adopted an earlier and less accurate version of the core field model which was available at the time. In the

present paper we adopt the entire spectrum of the best core field model for 1980 [*Langel and Estes,* 1985] and use the stringent magnetic anomaly map derived from POGO and Magsat data [*Arkani-Hamed et al.,* 1994] which has a lower error limit.

Before interpretation, it is important to emphasize that the magnetic susceptibility contrasts seen in Figure 7a are specified by spherical harmonics of degree 15-60, corresponding to wavelengths of about 2640-660 km. Magnetic bodies smaller than about 300 km in size are not resolved well. This low resolution is partly due to the global analysis which incorporates data from all over the world with vastly different quality. It is possible to achieve a resolution of about 400 km wavelength in a regional analysis [e.g., *Nakatsuka and Ono,* 1984] because of better control on the effects of nonlithospheric sources. This difference in resolution has minor effects on the prominent features seen in Figure 7a but would drastically change the shape and magnitude of small features. The severe limitation on the resolution actually arises from the satellite altitude of 400 km, which limits the use of satellite magnetic anomaly maps for detailed geological interpretation. However, the maps may provide good information about regional geology and tectonics, especially where no regional tectonic and geological maps are available.

It is worth reiterating that Figure 7a shows the vertically averaged magnetic susceptibility contrasts within a spherical shell of 40 km thickness that can give rise to the scalar magnetic anomalies seen in Figure 1. The average geothermal gradient indicates temperatures above 580°C (which is the Curie temperature of magnetite, the major magnetic mineral of the lithosphere) below a 40 km depth. Also, the Moho discontinuity in the continental lithosphere, which has been suggested as the base of the magnetic layer in the continents [*Wasilewski et al.,* 1979], is usually at about 40 km depth. In reality, the susceptibility contrasts in the lithosphere may arise from lateral variations in the magnetic susceptibility due to differences in iron content or in petrological and mineralogical conditions or from variations in the thickness of otherwise uniformly magnetized magnetic part of the lithosphere due to undulations of the Moho discontinuity or lateral temperature variations or from a combination of these factors. However, the vertically integrated susceptibility contrasts are the only quantity which can be determined using a satellite magnetic anomaly map (see Appendix B). Due to high altitudes, the satellite anomalies are insensitive to details of the vertical distribution of magnetization in the lithosphere [*Arkani-Hamed and Strangway,* 1985b]. It is a common consensus that the intermediate wavelength anomalies are of lower crustal origin in the continents [e.g., *Schnezler and Allenby,* 1983] but may also have contributions from the uppermost mantle in the oceanic areas [e.g., *Harrison and Carle,* 1981]. Variations in the thickness of the magnetic layer can be taken into account by simply scaling the susceptibility contrasts obtained for the 40-km-thick layer.

Also, Figure 7a shows the contrasts rather than the absolute magnetic susceptibility, the regions with positive/negative susceptibility contrasts are regarded as strongly/weakly magnetized areas, rather than being positively/negatively magnetized. This is due to the fact that a spherical shell of uniform magnetic susceptibility produces no magnetic anomaly when magnetized by an internal magnetic field such as the core field [*Runcorn,* 1975; *Harrison et al.,* 1986]. Consequently, a constant magnetic susceptibility, such as the annihilator adopted by *Hayling and Harrison* [1986] and *Harrison et al.* [1986], can be added to Figure 7a without affecting the resulting magnetic anomalies.

Detailed interpretation of individual features in Figure 7a is beyond the scope of this paper. We believe that Figure 7a provides useful constraints on the geophysical and geochemical processes that have produced these magnetic features. The data presented in Figures 1, 3a, and 7a are available (see the acknowledgments) for colleagues interested in detailed interpretation of certain features. In the following, we briefly discuss the geologic formations with common magnetic characteristics but only provide the locations of the well-defined magnetic anomalies which are associated with known geological features (Figure 6 and Table 1) without further interpretation of each individual feature.

Figure 7a shows that large magnetic susceptibility contrasts are found in both the continental and oceanic areas: the top seven highest contrasts are, in decreasing order, the Bangui anomaly, the anomaly northeast of South Georgia Island in the Southernmost Atlantic, the anomaly off South Africa, an anomaly in central South America, an anomaly off Antarctica south of Africa, the Kursk iron formation in Europe, and Mauritania in western Africa. Interestingly enough, three out of the seven largest magnetic susceptibility contrasts are located in oceanic areas, and they are associated with the KQZ in the conjugate area where the African, South American, and Antarctic plates separated.

The strong magnetic susceptibility contrasts in the continents emphasize the fact that continents are formed through tectonic processes that have juxtaposed blocks of vastly different magnetic properties. Distinct magnetic susceptibility contrasts are associated with the nuclei of Archean cratons, the continent-continent collision zones, the intracratonic basins, and the crustal rifts and aulacogens. The nuclei of many Archean cratons have high magnetization. The lack of well-defined magnetic anomalies associated with the Canadian shield is probably due to its great horizontal extent, such that major parts of its magnetic field overlap the core field and therefore are removed by the removal of the core field model in the process of deriving the satellite magnetic anomaly map. One possible reason for the strong magnetic signature of the nuclei is that the crust formed in the Archean is probably more magnetic due to the underplating of young and more magnetic oceanic lithosphere beneath micro continents. The vigorous convection in the high-temperature, low-viscosity mantle in the Archean resulted in faster seafloor spreading [*Hargraves,* 1986], reducing the average age of the

oceanic lithosphere to about 20 m.y. [*Bickle,* 1986]. The young, hot, and relatively buoyant (thus reluctant to subduct) oceanic lithosphere most likely underplated beneath the microcontinents and thickened the continental crust [*Hoffman and Ranalli,* 1988]. Based on the general characteristics of the age-dependent magnetization of the present oceanic lithosphere [*Bleil and Petersen,* 1983], it is plausible that the mean magnetization of the oceanic crust in Archean was stronger than at present. Alternatively, the strong magnetic anomalies of the nuclei of the Archean cratons may arise from their thicker magnetic layer. Due to presently low geothermal gradient in Archean shields [*Mercier,* 1980; *Chapman,* 1986], the Curie isotherm is deeper in these areas, and the magnetic part is probably thicker. It is possible to associate the magnetic anomaly of an Archean craton to the excess thickness of its magnetic crust and estimate the magnetic susceptibility of the lower crust in case the dimensions of the craton is known. However, this estimate should not be solely based on the assumption of a highly magnetic continental crust of uniform magnetic properties and attribute the lateral variations in the magnetization to a laterally varying geothermal gradient. Such an assumption may not be viable, because the surrounding collision zones are usually produced through strong tectonism caused by collision of blocks of lithosphere. It is quite possible that metamorphism and hydrothermal alteration of the crust in the collision zones have created hydrated, low-magnetic minerals [*Toft et al.,* 1993]. Moreover, thickening of the crust during collision and subsequent isostatic subsidence might have suppressed the strongly magnetic lower crust of the collision zones into the high-temperature upper mantle and have thermally demagnetized it. These collision-related processes may introduce lateral variations in the chemical and thus magnetic properties of the crust independent of the present temperature distribution.

Many young crustal rifts and aulacogens have low susceptibility, which may be explained by thermal demagnetization of the lower crust. The hot material intruded into the crust, especially into deeper parts of the crust, takes considerable amount of time to cool below the magnetic blocking temperatures of their minerals [*Arkani-Hamed and Strangway,* 1985a]. Thermal demagnetization is suggested as a viable mechanism for the low magnetization of the Basin and Range area in North America [*Mayhew,* 1985].

The oceanic areas younger than about 80 m.y. are characterized by relatively weaker magnetic susceptibility contrasts. This should not imply that the oceanic lithosphere is drastically less magnetic compared to the continental lithosphere. At satellite altitudes the oceanic lithosphere seems horizontally more homogeneous than the continental one (the high-frequency seafloor spreading magnetic anomalies decay below the noise level at high altitudes, except for the anomalies associated with the KQZ and over the areas where a given polarity period dominates), and consequently, it does not produce significant magnetic anomalies even if it is highly magnetized. It is worth mentioning that a horizontal layer of large extent with a laterally uniform magnetization produces no magnetic anomaly away from its edges regardless of the intensity of its magnetization. The KQZ in the North Atlantic Ocean, that off the Falkland plateau in South Atlantic Ocean, and that south of Africa and close to Antarctica in the Indian Ocean, are delineated by positive susceptibility contrasts. Figure 2 shows that the angle between the NRM and the present core field is less than 20° over these regions, suggesting that the inversion has introduced minor errors into their magnetization patterns. The lack of a distinct magnetic susceptibility contrast of the KQZ in the West Pacific Ocean is most likely due to the large extent of the zone that produces magnetic anomalies with major parts overlapping the core field. Like for the large continental shields, the removal of the core field in deriving the magnetic anomaly map has also removed the overlapping parts, the remaining parts delineate the edge effects [*Toft and Arkani-Hamed,* 1992]. Modeling the positive magnetic anomalies of the KQZ in the North Atlantic in terms of the NRM of the basaltic layer 2A [*LaBrecque and Raymond,* 1985] requires about 3 times more magnetization for the layer 2A of age about 80 m.y., suggesting that deeper magnetic sources, such as the NRM of the entire oceanic crust and probably the uppermost mantle have appreciable contribution to the anomalies [*Toft and Arkani-Hamed,* 1993]. There seems to be minor magnetic susceptibility contrasts associated with the ocean-continent boundary across passive margins. *Counil et al.* [1991] estimated an upper limit of 33,000 A for the ocean-continent bulk magnetization contrast, in good agreement with the value of 37,000 A resulted from studies of the aeromagnetic pattern off the east coast of North America [*Arkani-Hamed,* 1993], and the value 22,000 A required to explain the satellite magnetic anomaly of Rockall plateau associated with the bulk magnetization contrast between the continental lithosphere of the plateau and the surrounding oceanic lithosphere [*Toft and Arkani-Hamed,* 1993]. Other geological features such as the oceanic plateaus and microcontinents, parts of the mid-oceanic ridges, and some of the subduction zones have pronounced magnetic susceptibility contrasts. These detailed features are not discussed here.

Appendix A: Calculations of the Coupling Terms

There are two coupling terms, A and W, appearing in the inversion formulas. The term A,

$$A = \Gamma\, \delta\mathbf{b} \cdot \nabla V, \tag{A1}$$

appears in the relationship between the magnetic potential V and the observed magnetic anomaly T. It arises from the fact that the unit vector of the geomagnetic field, $\mathbf{b}$, deviates from its dipole component, $\mathbf{b}_1$,

because of the contribution from the nondipole parts of the field, $\delta\mathbf{b}$. The function Γ in the right-hand side of (A1) is defined in the text. A is calculated in the space domain at $0.5^\circ \times 0.5^\circ$ latitude and longitude grid points at each iteration. This amounts to determining $\delta\mathbf{b}, \Gamma$, and ∇V at the grid points and performing the dot product in the space domain. ∇V is first calculated analytically by taking the gradient of (6).

The coupling term W,

$$W = \frac{1}{4\pi}\int \sigma(\theta_o,\phi_o)\,\delta\mathbf{B}(\theta_o,\phi_o)\cdot\nabla_o\frac{1}{|\mathbf{r}-\mathbf{r}_o|}dv_o, \quad \text{(A2)}$$

represents the magnetic potential of the lithosphere which is magnetized by the nondipole part of the geomagnetic field. W is evaluated in the spherical harmonic domain as follows. Let

$$\mathbf{\Psi} = \sigma(\theta_o,\phi_o)\,\delta\mathbf{B}(\theta_o,\phi_o), \quad \text{(A3)}$$

and expand this vector in spherical harmonics as

$$\mathbf{\Psi} = \sum_{k=1}^{N}\sum_{l=0}^{k}\left[\begin{pmatrix}\psi_{kl}^{r,e}\\ \psi_{kl}^{\theta,e}\\ \psi_{kl}^{\phi,e}\end{pmatrix}\cos(l\phi_o) + \begin{pmatrix}\psi_{kl}^{r,o}\\ \psi_{kl}^{\theta,o}\\ \psi_{kl}^{\phi,o}\end{pmatrix}\sin(l\phi_o)\right]P_k^l(\cos\theta_o), \quad \text{(A4)}$$

where $(\psi_{kl}^{r,e},\psi_{kl}^{r,o})$, $(\psi_{kl}^{\theta,e},\psi_{kl}^{\theta,o})$, and $(\psi_{kl}^{\phi,e},\psi_{kl}^{\phi,o})$ are the spherical harmonic coefficients of the r,θ, and ϕ components of $\mathbf{\Psi}$, respectively. Also expand the function $\frac{1}{|\mathbf{r}-\mathbf{r}_o|}$ and W in terms of spherical harmonics as

$$\frac{1}{|\mathbf{r}-\mathbf{r}_o|} = \sum_{n=0}^{N}\frac{r_o^n}{r^{n+1}}\sum_{m=0}^{n}(\cos m\phi\cos m\phi_o + \sin m\phi\sin m\phi_o)\,P_n^m(\cos\theta)P_n^m(\cos\theta_o), \quad \text{(A5)}$$

$$W = \sum_{n=1}^{N}\frac{a^{n+2}-R_1^{n+2}}{r^{n+1}}\sum_{m=0}^{n}(W_{nm}^e\cos m\phi + W_{nm}^o\sin m\phi)\,P_n^m(\cos\theta), \quad \text{(A6)}$$

Putting (A3) - (A6) into (A2) and using the orthogonality of the spherical harmonics, we obtain the following expression for the spherical harmonic coefficients of W:

$$W_{nm}^e = \frac{1}{4(n+2)}\left[n\sum_{k=1}^{N}\psi_{km}^{r,e}(1+\delta^{m0})R_{kn}^m + \sum_{k=1}^{N}\psi_{km}^{\theta,e}(1+\delta^{m0})Q_{kn}^m - m\sum_{k=1}^{N}\psi_{km}^{\phi,e}(1-\delta^{m0})S_{kn}^m\right], \quad \text{(A7a)}$$

and

$$W_{nm}^o = \frac{1}{4(n+2)}\left[n\sum_{k=1}^{N}\psi_{km}^{r,o}(1-\delta^{m0})R_{kn}^m + \sum_{k=1}^{N}\psi_{km}^{\theta,o}(1-\delta^{m0})Q_{kn}^m + m\sum_{k=1}^{N}\psi_{km}^{\phi,o}(1+\delta^{m0})S_{kn}^m\right], \quad \text{(A7b)}$$

where

$$R_{kn}^m = \int P_k^m(\cos\theta)\,P_n^m(\cos\theta)\sin\theta d\theta, \quad \text{(A8a)}$$

$$Q_{kn}^m = \int P_k^m(\cos\theta)\frac{dP_n^m(\cos\theta)}{d\theta}\sin\theta d\theta, \quad \text{(A8b)}$$

$$S_{kn}^m = \int \frac{1}{\sin\theta}P_k^m(\cos\theta)\,P_n^m(\cos\theta)\sin\theta d\theta, \quad \text{(A8c)}$$

and δ^{m0} is the Kronecker delta function.

Appendix B: Nonuniqueness of the Inversion Processes

This appendix is concerned with the nonuniqueness of the inversion processes employed in this paper in order to convert a global scalar magnetic anomaly map into a global magnetic potential map and to convert the potential map into a global magnetic susceptibility contrast map.

Potential

The basic relationship between the scalar magnetic anomaly T and the magnetic potential V of a body is

$$T = -\mathbf{b}\cdot\nabla V. \quad \text{(B1)}$$

in which $\mathbf{b}$ is the unit vector in the core field direction. The inversion problem is to determine V knowing T. Let V_1 be a solution to (B1), then $V_2 = V_1 + V_o$ is also a solution, where V_o is the solution of the homogenous equation

$$\mathbf{b}\cdot\nabla V_o = 0 \quad \text{(B2)}$$

∇V_o is a vector field lying on the equipotential surfaces of the geomagnetic potential. V_o can be determined formally as follows. Multiplying (B2) by the magnitude of the core field (a nonzero function) changes $\mathbf{b}$ into the core field, $\mathbf{B}$, which is equal to the gradient of the geomagnetic potential G. Equation (B2) is thus transformed into

$$\nabla G\cdot\nabla V_o = 0. \quad \text{(B3)}$$

Now, expand both G and V_o in terms of the fully normalized spherical harmonics,

$$G = \sum_{nm}G_{nm}(r)Y_{nm}(\theta,\phi), \quad \text{(B4)}$$

$$V_o = \sum_{pq} U_{pq}(r) Y_{pq}(\theta, \phi). \quad \text{(B5)}$$

Throughout this appendix, $\sum_{ij}$ denotes summation over $i = 0, ..., N$ (N is the highest degree considered) and $j = -i, ..., +i$. $Y_{ij}(\theta, \phi)$ is the fully normalized spherical harmonic of degree i and order j [*Edmonds*, 1960], θ is the colatitude, ϕ is the east longitude, and G_{nm} and U_{pq} are the expansion coefficients which are complex functions and depend on r, the distance from Earth's center to the observation point. Putting (B4) and (B5) into (B3) yields

$$\sum_{nm}\sum_{pq}\left[\frac{dG_{nm}}{dr}\frac{dU_{pq}}{dr}Y_{nm}Y_{pq} + \frac{G_{nm}U_{pq}}{r^2}\left(\frac{\partial Y_{nm}}{\partial\theta}\frac{\partial Y_{pq}}{\partial\theta} + \frac{1}{\sin^2\theta}\frac{\partial Y_{nm}}{\partial\phi}\frac{\partial Y_{pq}}{\partial\phi}\right)\right] = 0. \quad \text{(B6)}$$

Both G and V_o are magnetic potentials of internal origin for magnetic measurements above the surface. Therefore we can write

$$G_{nm} = \frac{1}{r^{n+1}}G'_{nm}, \quad U_{pq} = \frac{1}{r^{p+1}}U'_{pq}, \quad \text{(B7)}$$

where G'_{nm} and U'_{pq} are complex constants. Now putting (B7) into (B6) and expressing the derivatives of Y_{nm} and Y_{pq} in terms of spherical harmonics yields

$$\sum_{nm}\sum_{pq}\frac{1}{r^{n+p+4}}\left(\alpha^{pq}_{nm}\,G'_{nm}U'_{pq} + \beta^{pq}_{nm}G'_{n,m+1}U'_{p,q-1} + \beta^{nm}_{pq}\,G'_{n,m-1}U'_{p,q+1}\right)Y_{nm}Y_{pq} = 0, \quad \text{(B8)}$$

where

$$\alpha^{pq}_{nm} = 2\left[(n+1)(p+1) - mq\right],$$

$$\beta^{pq}_{nm} = -\left[(n+m+1)(n-m)(p-q+1)(p+q)\right]^{1/2}.$$

Equation (B8) holds at any arbitrary point (r, θ, ϕ). This requires that

$$\alpha^{pq}_{nm}\,G'_{nm}U'_{pq} + \beta^{pq}_{nm}G'_{n,m+1}U'_{p,q-1} + \beta^{nm}_{pq}\,G'_{n,m-1}U'_{p,q+1} = 0. \quad \text{(B9)}$$

In (B9) the coefficients $G'_{n,m-1}, G'_{nm}$, and $G'_{n,m+1}$ are known, and the unknown coefficients $U'_{p,q-1}, U'_{pq}$, and $U'_{p,q+1}$ are linearly coupled. Noting that $U'_{pq} = 0$ for $|q| > p$, the coefficients of the harmonics of degree p are determined in terms of the coefficient of the sectorial harmonic U'_{pp}, which has an arbitrary value. The homogeneous solution consist of an infinite series of spherical harmonics. For a dipolar core field, (B9) is reduced to the *Backus* [1970] series [*Arkani-Hamed and Strangway*, [1985b].

Susceptibility

Consider a magnetic spherical shell of the inner radius R_1 and outer radius a having induced magnetization. The relationship between its magnetic susceptibility, $\sigma(\mathbf{r}_o)$, and magnetic potential, $V(\mathbf{r})$, is

$$V(\mathbf{r}) = \frac{1}{4\pi}\int \sigma(\mathbf{r}_o)\mathbf{B}(\mathbf{r}_o)\cdot\nabla_o\frac{1}{|\mathbf{r}-\mathbf{r}_o|}dv_o, \quad \text{(B10)}$$

Now expand $\sigma(\mathbf{r}_o)$ and $\frac{1}{|\mathbf{r}-\mathbf{r}_o|}$ in terms of spherical harmonics as

$$\sigma(\mathbf{r}_o) = \sum_{pq}\sigma_{pq}(r_o)Y_{pq}(\theta_o, \phi_o), \quad \text{(B11)}$$

$$\frac{1}{|\mathbf{r}-\mathbf{r}_o|} = \sum_{kl}\left(\frac{4\pi}{2k+1}\right)\left(\frac{r_o^k}{r^{k+1}}\right)Y_{kl}(\theta,\phi)Y^*_{kl}(\theta_o,\phi_o), \quad \text{(B12)}$$

and note that

$$\mathbf{B}(\mathbf{r}_o) = -\nabla_o G, \quad \text{(B13)}$$

and let

$$G_{nm}(r_o) = g_{nm}\frac{r_c^n}{r_o^{n+1}} \quad \text{(B14)}$$

where $\sigma_{pq}(r_o)$ is a function of distance from Earth's center to the volume element of the magnetic body located at r_o, r_c is the radius of the core, and g_{nm} is a complex constant. In (B12) r is assumed to be greater than r_o. Putting (B4), (B11)-(B14) into (B10) and after some manipulations, we obtain

$$V(\mathbf{r}) = -\sum_{kl}\frac{4\pi}{(2k+1)r^{k+1}}\sum_{nm}g_{nm}\sum_{pq}\left[-k(n+1)J^{lqm}_{kpn} + F^{lqm}_{kpn}\right]\left[\int\sigma_{pq}(r_o)r_o^{k-n-1}dr_o\right]Y_{kl}(\theta,\phi), \quad \text{(B15)}$$

in which the coupling coefficients J^{lqm}_{kpn} and F^{lqm}_{kpn} are defined as

$$J^{lqm}_{kpn} = \int Y_{pq}Y_{nm}Y^*_{kl}d\Omega, \quad \text{(B16a)}$$

$$F^{lqm}_{kpn} = \int Y_{pq}\left(\frac{\partial Y_{nm}}{\partial\theta}\frac{\partial Y^*_{kl}}{\partial\theta} + \frac{1}{sin^2\theta}\frac{\partial Y_{nm}}{\partial\phi}\frac{\partial Y^*_{kl}}{\partial\phi}\right)d\Omega. \quad \text{(B16b)}$$

They are determined in terms of Wigner's 3-J symbols [see *Arkani-Hamed and Toksoz*, 1984, Appendix A]. $d\Omega$ denotes the surface element on the sphere. Now let σ^1_{pq} give rise to the observed potential, then $\sigma^2_{pq} = \sigma^1_{pq} + \sigma^o_{pq}$ will also satisfy the observed potential provided that substitution of σ_{pq} in (B15) by σ^o_{pq} makes the right-hand side of the equation zero everywhere. This happens when the first or the second bracket in the right-hand side vanishes. Setting the second bracket to zero provides a particular σ^o_{pq} which makes the integral vanish. The integral is a moment of rank $j = k-n-1$ of σ^o_{pq} about the center, $r = 0$, and should vanish for all values of $k = 0, ..., \infty$ and $n = 1, ...13$. Therefore σ^o_{pq} must always be zero, strictly speaking, and the nonuniqueness of the magnetic susceptibility does not arise from vanishing of the second bracket in (B15). In practice, however, k is limited because of the restricted resolution of the magnetic potential due to satellite altitudes. The most recent satellite magnetic anomaly map has a resolution corresponding to a k value of 65 [*Ravat et al.*, 1995]. For these limited k values the weighting function r^j in the integral is a very slowly varying function

within the surface layer of thickness $D = 40$ km, and the integral can be expressed as

$$\int_{R_1}^{a} \sigma^o_{pq}(r_o)\, r_o^j\, dr_o = R_1^j \int_0^D \sigma^o_{pq}(x) \left(1 + \frac{x}{R_1}\right)^j dx$$
$$= R_1^j \left[\int_0^D \sigma^o_{pq}(x)dx + \frac{j}{R_1} \int_0^D \sigma^o_{pq}(x)x dx \right.$$
$$\left. + \frac{j(j-1)}{2R_1^2} \int_0^D \sigma^o_{pq}(x)x^2 dx \right] = 0 \qquad \text{(B17)}$$

where only the first three terms of the binomial expansion of $(1 + x/R_1)^j$ are retained. The terms ignored are less than 1% of the leading term even for the maximum values of j (=65) and x ($=D$). Therefore in practice it is sufficient that only the first three moments of σ^o_{pq} vanish, and the solution of (B17) becomes

$$\sigma^o_{pq} = x^3 - \frac{3}{2}Dx^2 + \frac{6}{10}D^2x - \frac{1}{20}D^3. \qquad \text{(B18)}$$

A surface layer of thickness about 40 km with a reasonable magnetic susceptibility that is proportional to σ^o_{pq} produces no appreciable magnetic potential at satellite altitudes for any arbitrary p and q values.

Putting the first bracket in the right-hand side of (B15) to zero,

$$k\,(n+1)\, J^{lqm}_{kpn} - F^{lqm}_{kpn} = 0, \qquad \text{(B19)}$$

defines those spherical harmonics of the magnetic susceptibility contrasts which produce no magnetic potential regardless of the radial dependence of the contrasts. The simplest one is the zeroth degree harmonic, $p = q = 0$, i.e., a magnetic layer with laterally uniform magnetic susceptibility. In this case the left-hand side of (B19) is reduced to

$$k(n+1) \int Y^*_{nm} Y_{kl}\, d\Omega - \int \left(\frac{\partial Y^*_{nm}}{\partial \theta} \frac{\partial Y_{kl}}{\partial \theta} \right.$$
$$\left. + \frac{1}{sin^2\theta} \frac{\partial Y^*_{nm}}{\partial \phi} \frac{\partial Y_{kl}}{\partial \phi} \right) d\Omega. \qquad \text{(B20)}$$

Expressing the integrant of the second integral in terms of spherical harmonics [see *Arkani-Hamed and Toksoz*, 1984, Appendix A], using the orthogonality of the spherical harmonics,

$$\int Y^*_{nm} Y_{kl}\, d\Omega = \delta^{ml}_{nk} \qquad \text{(B21)}$$

where the Kronecker delta function δ^{ml}_{nk} equals to 1 for $n = k$ and $m = l$, and to zero otherwise, and taking in to account the following relationship:

$$Y^*_{nm} = (-1)^m\, Y_{n,-m} \qquad \text{(B22)}$$

show that the expression in (B20) vanishes. Note that in this example the magnetic layer does not need to have a uniform susceptibility, rather it is required to have a laterally uniform susceptibility while changing arbitrarily in the radial direction. A simplified version of this example is when the layer has a uniform magnetic susceptibility, which is the case considered by *Runcorn* [1975], and *Hayling and Harrison* [1986] referred to this constant susceptibility as an annihilator.

There seems to be no nontrivial p and q values to make (B19) vanish for all values of k, l, n, and m, unless both J^{lqm}_{kpn} and F^{lqm}_{kpn} vanish separately. On the basis of the selection rules of the 3-J symbols, this occurs only when p is greater than the maximum value of $n + k$, specifying harmonics of degree much higher than the resolution of magnetic anomaly maps and thus not interesting.

Acknowledgments. This research was supported by the Natural Sciences and Engineering Research Council of Canada (NSERC) grant OGP0041245, and by the attribution of an NSERC International Fellowship to J.D. We acknowledge the invaluable contribution of Choi Yujin in writing the computer codes to compute the potential and susceptibility maps. We would like to thank J. Cain and D. Ravat for allowing us to use the spherical harmonic coefficients of their models which were kindly given to us by M. Purucker, and we thank Y. Cohen for providing us with his ΔZ and ΔX component maps. Many of the comments made by the Associate Editor, Carol Raymond, and two anonymous reviewers were constructive and we would like to thank them for reviewing the paper. We also thank P. Wessel and W. Smith for providing the GMT software used to make the maps, and P. Turner for the Xmgr software used to draw the graphics. Data from Figures 1, 3a, and 7a will be provided on a 0.5° × 0.5° grid and also as sets of spherical harmonic coefficients upon request.

References

Arkani-Hamed, J., The bulk magnetization contrast across the ocean-continent boundary in the east coast of North America, *Geophys. J. Int., 115,* 152-158, 1993.

Arkani-Hamed, J., and G. Celetti, Effects of thermal remanent magnetization on the magnetic anomalies of intrusives, *J. Geophys. Res., 94,* 7364-7378, 1989.

Arkani-Hamed, J., and W.J. Hinze, Limitations of the long-wavelength components of the North American magnetic anomaly map, *Geophysics, 55,* 1577-1588, 1990.

Arkani-Hamed, J., and D.W. Strangway, An interpretation of magnetic signatures of aulacogens and cratons in Africa and South America, *Tectonophysics, 113,* 257-269, 1985a.

Arkani-Hamed, J., and D.W. Strangway, Lateral variations of apparent magnetic susceptibility of lithosphere deduced from Magsat data, *J. Geophys. Res., 90,* 2655-2664, 1985b.

Arkani-Hamed, J., and D.W. Strangway, Band-limited global scalar magnetic anomaly map of the Earth derived from Magsat data, *J. Geophys. Res., 91,* 8193-8203, 1986.

Arkani-Hamed, J., and M.N. Toksoz, Thermal evolution of Venus, *Phys. Earth Planet. Inter., 34,* 232-250, 1984.

Arkani-Hamed, J., A.L. Langel, and M. Purucker, Scalar magnetic anomaly maps of Earth derived from POGO and Magsat data, *J. Geophys. Res., 99,* 24075-24090, 1994.

Backus, G.E., Non-uniqueness of the external geomagnetic field determined by surface intensity measurements, *J. Geophys. Res., 75,* 6339-6341, 1970.

Beck, F., Courbes de dérive des pôles du Permien à l'actuel

pour les continents péri-Atlantiques et Indiens: confrontation avec les reconstructions paléogéographiques, Ph.D. thesis, Univ. L. Pasteur, Strasbourg, France, 222 pp., 1994.

Bickle, M.J., Implications of melting for stabilization of the lithosphere and heat loss in the Archean Earth, *Earth Planet. Sci. Lett., 80,* 314-324, 1986.

Bleil, U., and N. Petersen, Variations in magnetization intensity and low-temperature titanomagnetite oxidation of ocean floor basalts, *Nature, 301,* 384-388, 1983.

Bradley, L.M., and H. Frey, Constraints on the crustal nature and tectonic history of the Kerguelen plateau from comparative magnetic modelling using Magsat data, *Tectonophysics, 145,* 243-251, 1988.

Cain, J.C., Z. Wang, D.R. Schmitz, and J. Meyer, The geomagnetic spectrum for 1980 and core-crustal separation, *Geophys. J., 97,* 443-447, 1989.

Chapman, D.S., Thermal gradients in the continental crust, in *The Nature of the Lower Continental Crust, Geol. Soc. Spec. Publ., London, 24,* 63-70, 1986.

Cohen, Y., and J. Achache, New global vector magnetic anomaly maps derived from Magsat data, *J. Geophys. Res.,* 95, 10,783-10,800, 1990.

Counil, J.L., Y. Cohen, and J. Achache, The global continent-ocean magnetization contrasts, *Earth Planet. Sci. Lett., 103,* 354-364, 1991.

Dyment, J., and J. Arkani-Hamed, Remanent magnetic anomaly of the world's oceans at satellite altitude, *EoS Trans. AGU, 75* (44), Fall Meet. Suppl., 197, 1994.

Edmonds, A.R., *Angular Momentum in Quantum Mechanics,* pp. 45-52, University Press, Princeton, N.J., 1960.

Frey, H., Magsat scalar anomaly distribution: The global perspective, *Geophys. Res. Lett., 9,* 277-280, 1982.

Frey, H., Magsat and POGO magnetic anomalies over the Lord Howe Rise: Evidence against a simple continental crustal structure, *J. Geophys. Res., 90,* 2631-2639, 1985.

Friis-Christensen, E., The Oersted mission: Objectives and international cooperation, paper presented at the First Oersted International Science Team Meeting, Danish Meteorological Institute, Copenhagen, 1995.

Fullerton, L.G., H.V. Frey, J.H. Roark, and H.H. Thomas, Evidence for a remanent contribution in Magsat data from the Cretaceous quiet zone in the South Atlantic, *Geophys. Res. Lett., 16,* 1085-1088, 1989.

Fullerton, L.G., H.V. Frey, J.H. Roark, and H.H. Thomas, Contribution of Cretaceous quiet zone natural remanent magnetization to Magsat anomalies in the Southwest Indian Ocean, *J. Geophys. Res., 99,* 11,923-11,936, 1994.

Grauch, V.J.S., Limitations on digital filtering of the DNAG magnetic data set for the conterminous U.S., *Geophysics, 58,* 1281-1296, 1993.

Hargraves, R.B., Faster spreading of greater ridge length in the Archean?, *Geology, 14,* 750-752, 1986.

Harrison, C.G.A., and H.M. Carle, Intermediate wavelength magnetic anomalies over ocean basins, *J. Geophys. Res., 86,* 11,585-11,599, 1981.

Harrison, C.G.A., H.M. Calre, and K.L. Hayling, Interpretation of satellite elevation magnetic anomalies, *J. Geophys. Res., 91,* 3633-3650, 1986.

Hayling, K.L., and C.G.A. Harrison, Magnetization modelling in the North Atlantic using Magsat data, *J. Geophys. Res., 91,* 12,423-12,443, 1986.

Hinze, W.J., and Committee for the Magnetic Anomaly Map of North America, Magnetic anomaly map of North America, *Leading Edge, 7,* 19-21, 1988.

Hoffman, P.F., and G. Ranalli, Archean oceanic flake Tectonics, *Geophys. Res. Lett., 15,* 1077-1080, 1988.

Johnson, B.D., Viscous remanent magnetization model for the Broken Ridge satellite magnetic anomaly, *J. Geophys., Res., 90,* 2640-2646, 1985.

LaBrecque, J.L., and S.C. Cande, Intermediate-wavelength magnetic anomalies over the central Pacific, *J. Geophys. Res., 89,* 11,124-11,134, 1984.

LaBrecque, J.L., and C.A. Raymond, Seafloor spreading anomalies in the Magsat field, *J. Geophys. Res., 90,* 2565-2575, 1985.

Langel, R.A., Global magnetic anomaly maps derived from POGO spacecraft data, *Phys. Earth Planet. Inter., 62,* 208-230, 1990.

Langel, R.A., and R.H. Estes, The near-earth magnetic field at 1980 determined from Magsat data, *J. Geophys. Res., 90,* 2495-2509, 1985.

Langel, R.A., J.D. Phillips, and R.J. Horner, Initial scalar magnetic anomaly map from Magsat, *Geophys. Res. Lett., 9,* 269-272, 1982a.

Langel, R.A., G.W. Ousley, J. Berbert, The Magsat mission, *Geophys. Res. Lett., 9,* 243-245, 1982b.

Langel, R.A., B.J. Benson, R.M. Orem, The Magsat Bibliography (revision 1), *NASA Tech. Memo., Tm-100776,* 1991.

Mayhew, M.A., Inversion of satellite magnetic anomaly data, *J. Geophys., 45,* 119-128, 1979.

Mayhew, M.A., Curie isotherm surfaces inferred from high-altitude magnetic anomaly data, *J. Geophys. Res., 90,* 2647-2654, 1985.

Mayhew, M.A., B.D. Johnson, and R.A. Langel, An equivalent source model of the satellite-altitude magnetic anomaly field over Australia, *Earth Planet. Sci. Lett., 51,* 189-198, 1980.

Mercier, J.-C., Single-pyroxene thermobarometry, *Tectonophysics, 70,* 1-37, 1980.

Mueller, R.D., W.R. Roest, J.-Y. Royer, L.M. Gahagan, and J.G. Sclater, A digital age map of the ocean floor, *Scripps Inst. of Oceanogr. Ref. Ser., 93-30,* 1994.

Nakatsuka, T., and Y. Ono, Geomagnetic anomalies over the Japanese Islands region derived from Magsat data, *J. Geomagn. Geoelectr., 36,* 455-462, 1984.

Pal, P.C., The Indian Ocean Magsat anomalies and strong geomagnetic field during Cretaceous "quiet" zone, *Phys. Earth Planet. Inter., 64,* 279-289, 1990.

Plates Project, Atlas of geographic reconstructions (present-day to 600 Ma), *Prog. Rep. 60-1293,* 61 pp., Univ. of Tex. Inst. for Geophys., Austin, 1993.

Ravat, D., R.A. Langel, M. Purucker, J. Arkani-Hamed, and D.E. Alsdorf, Revised vector and scalar Magsat magnetic anomaly maps, *J. Geophy. Res., 100,* 20,111-20,136, 1995.

Regan, R.D., J.C. Cain, and W.M. Davis, A global magnetic anomaly map, *J. Geophys. Res., 80,* 794-802, 1975.

Royer, J.Y., R.D. Mueller, L.M. Gahagan, L.A. Lawver, C.L. Mayes, D. Nuernberg, and J.G. Sclater, A global isochron chart, *Tech. Rep. 117,* 38 pp., Univ. of Tex. Inst. for Geophys., Austin, 1992.

Runcorn, S.K., On the interpretations of lunar magnetism, *Phys. Earth Planet. Inter., 10,* 327-335, 1975.

Schnetzler, C.C., and R.J. Allenby, Estimation of lower crustal magnetization from satellite derived anomaly field, *Tectonophysics, 93,* 33-45, 1983.

Toft, P.B., and J. Arkani-Hamed, Magnetization of the Pacific ocean lithosphere deduced from Magsat data, *J. Geophys. Res., 97,* 4387-4406, 1992.

Toft, P.B., and J. Arkani-Hamed, Induced magnetization of the oceanic lithosphere and ocean-continent magnetization contrast inferred from Magsat anomalies, *J. Geophys. Res., 98,* 6267-6282, 1993.

Toft, P.B., P.A.H. Scowen, J. Arkani-Hamed, and D. Francis, Demagnetization by hydration in deep-crustal rocks in

the Grenville province of Quebec, Canada: Implications for magnetic anomalies of continental collision zones, *Geology, 21,* 999-1002, 1993.

Wasilewski, P.J., H.H. Thomas, and M.A. Mayhew, The Moho as magnetic boundary, *Geophys. Res. Lett., 6,* 541-544, 1979.

Yanagisawa, M., and M. Kono, Mean ionospheric field correction for Magsat data, *J. Geophys. Res., 90,* 2527-2536, 1985.

Ziegler, A.M., C.R. Scotese, and S.F. Barett, Mesozoic and Cenozoic paleogeographic maps, in *Tidal Friction and the Earth Rotation II,* Edited by P. Brosche and J. Sunderman, pp. 240-252, Springer-Verlag, Berlin, 1983.

J. Arkani-Hamed, Earth and Planetary Sciences, McGill University, 3450 University St., Montréal, QC H3A-2A7, Canada. (e-mail: jafar@planet.eps.mcgill.ca)

J. Dyment, URA 1278 et GDR GEDO, Université de Bretagne Occidentale, BP 809, 6 Avenue Le Gorgeu, 29285 Brest Cedex, France. (e-mail: jerome@univ-brest.fr)

(Received June 28, 1995; revised November 9, 1995; accepted November 14, 1995.)